J. Fluid Mech. (2017), *vol.* 825, *pp.* 245–283. © Cambridge University Press 2017
doi:10.1017/jfm.2017.366

Three-dimensionality of elliptical cylinder wakes at low angles of incidence

Anirudh Rao[1], Justin S. Leontini[2], Mark C. Thompson[1,†] and Kerry Hourigan[1]

[1]Fluids Laboratory for Aeronautical and Industrial Research (FLAIR), Department of Mechanical and Aerospace Engineering, 17 College Walk, Monash University, Clayton, Victoria 3800, Australia

[2]Department of Mechanical and Product Design Engineering, Swinburne University of Technology, John Street, Hawthorn, Victoria 3122, Australia

(Received 8 October 2016; revised 19 March 2017; accepted 23 May 2017;
first published online 20 July 2017)

The wake of an elliptical cylinder at low incident angles is investigated for different aspect ratio ($\Gamma =$ major:minor axis ratio) cylinders using stability analysis and direct simulations. In particular, two- and three-dimensional transitions are mapped for cylinders of aspect ratios between 1 and 4 using Floquet stability analysis. The transition scenario for near-unity aspect ratio cylinders resembles that for a circular cylinder wake as Reynolds number is increased to $Re \lesssim 400$; first, with the transition from steady two-dimensional flow to unsteady two-dimensional flow, followed by the onset of three-dimensional flow via a long-wavelength instability (mode A), then, a short-wavelength instability (mode B) and, finally, an intermediary wavelength instability which is quasi-periodic in nature (mode QP). The effect of the incident angle on this transition scenario for the low-aspect-ratio cylinders is minimal. As the aspect ratio is increased towards 2, two synchronous modes, modes $\widehat{\mathrm{A}}$ and $\widehat{\mathrm{B}}$, become unstable; these modes have spatio-temporal symmetries similar to their circular cylinder wake counterparts, modes A and mode B, respectively. While mode $\widehat{\mathrm{A}}$ persists for all incident angles investigated here, mode $\widehat{\mathrm{B}}$ is found only to be unstable for incident angles up to 10°. Surprisingly, for $1.8 \lesssim \Gamma \lesssim 2.9$, the mode A instability observed at zero incident angle emerges as a quasi-periodic mode as the incident angle is increased even slightly. At higher incident angles, this quasi-periodic mode once again transforms to a real mode on increasing the Reynolds number. The parameter space maps for the various aspect ratios are presented in the Reynolds number–incident angle plane, and the three-dimensional modes are discussed in terms of similarities to and differences from existing modes. A key aim of the work is to map the different modes and various transition sequences as a simple body geometry is systematically changed and as the flow symmetry is systematically broken; thus, insight is provided on the overall path towards fully turbulent flow.

Key words: parametric instability, vortex shedding, wakes

1. Introduction

Flow past elliptical cylinders for varying angles of incidence is investigated for various aspect ratios at low Reynolds numbers. Here, the Reynolds number is defined

† Email address for correspondence: mark.thompson@monash.edu

by $Re = UD/\nu$, where U is the incoming flow velocity, D is the minor axis of the elliptical cylinder with the major axis aligned with the flow and ν is the kinematic viscosity. The aspect ratio (Γ) of the elliptical cylinder is the ratio of the major axis (a) to the minor axis (D). For a circular cylinder, the aspect ratio is unity with the major and minor axis being the diameter. The focus of this study is to explore the two- and three-dimensional transitions that occur for $\Gamma \geqslant 1$ at low angles of incidence (I).

The various flow transitions that occur in the wake of a circular cylinder have been investigated experimentally by Williamson (1996*a*) and numerically by Karniadakis & Triantafyllou (1992), Barkley & Henderson (1996), Thompson, Hourigan & Sheridan (1996), Barkley, Tuckerman & Golubitsky (2000), Akbar, Bouchet & Dušek (2011), Jiang *et al.* (2016*a*,*b*), amongst others. At $Re \simeq 46$, the flow transitions from a steady state to an unsteady state that is characterised by the alternate shedding of vortices from each side of the cylinder, is commonly known as Bénard–von Kármán (BvK) shedding. As the Reynolds number is increased to $\simeq$190, spanwise undulations are observed in the wake with a wavelength of $\simeq 4D$. This three-dimensional instability is known as mode A and was first observed experimentally by Williamson (1988) and predicted numerically based on Floquet stability analysis by Barkley & Henderson (1996). As the Reynolds number is increased, a smaller wavelength instability appears in the flow with a spanwise wavelength of $\simeq 0.8D$, which is termed mode B. Barkley & Henderson (1996) observed the onset of mode B instability to occur around $Re \simeq 259$, while it was observed to occur at much lower Reynolds numbers in the experiments. This is due to the instability mode becoming unstable on an already three-dimensional base flow. Modes A and B are synchronous modes whose periods are commensurate with the period of the base flows, and have also been observed in other bluff body wakes from cylinders with different cross-sections (Robichaux, Balachandar & Vanka 1999; Leontini, Lo Jacono & Thompson 2015). Three-dimensional modes that are not commensurate with the base flow periods have also been observed in the bluff body wakes and are known as quasi-periodic (QP) modes (Blackburn & Lopez 2003; Marques, Lopez & Blackburn 2004; Blackburn, Marques & Lopez 2005; Blackburn & Sheard 2010). These modes have been observed to occur at Reynolds numbers beyond the onset of modes A and B (Blackburn *et al.* 2005; Leontini, Thompson & Hourigan 2007; Leontini *et al.* 2015), and they often seem to be almost subharmonic. True subharmonic modes have also been observed in the wake of tori (Sheard, Thompson & Hourigan 2004*a*,*b*), rotating cylinders (Radi *et al.* 2013; Rao *et al.* 2013*a*, 2015*a*), rotating (and non-rotating) cylinders near walls (Rao *et al.* 2015*c*; Jiang *et al.* 2017), square cylinders when the incoming flow is at an angle of incidence (Sheard, Fitzgerald & Ryan 2009; Sheard 2011), inclined flat plates (Yang *et al.* 2013), stalled airfoils (Meneghini *et al.* 2011), two staggered cylinders (Carmo *et al.* 2008) and when trip wires are placed in the vicinity of a circular cylinder (Zhang *et al.* 1995; Yildirim, Rindt & van Steenhoven 2013*a*,*b*; Rao *et al.* 2015*b*). In these cases there is a geometry/flow change that breaks the centreplane-reflection/half-period translation symmetry of the BvK wake base flow (Blackburn *et al.* 2005).

Johnson, Thompson & Hourigan (2004) investigated the wake behind elliptical cylinders for $\Gamma \leqslant 1$ at low Reynolds numbers and observed a low-frequency secondary wake that develops downstream of the BvK-like shedding at low aspect ratios. An extension to this study was carried out by Thompson *et al.* (2014), who carried out Floquet stability analysis and observed the onset of three-dimensionality via mode A-type instability. The onset of mode A instability decreased from $Re_c = 190.3$ at $\Gamma = 1$ to $Re_c = 88.5$ at $\Gamma = 0.25$. Furthermore, mode A was found to become only

marginally stable at lower aspect ratios of $\Gamma = 0.1$. While many studies (Lindsey 1937; Lugt & Haussling 1972; Nair & Sengupta 1997; Badr, Dennis & Kocabiyik 2001; Mori, Yoshikawa & Ota 2003; Kim & Park 2006; Yoon *et al.* 2016) have investigated the flow past elliptical cylinders for $\Gamma > 1$ at higher Reynolds numbers, very few studies have detailed the two- and three-dimensional transitions that occur in the wake of elliptical cylinders at low Reynolds numbers, other than the recent study of Leontini *et al.* (2015).

Kim & Sengupta (2005) performed two-dimensional simulations of the flow past low-aspect-ratio elliptical cylinders for $0.83 \leqslant \Gamma \leqslant 1.25$ at zero angle of incidence for $Re \leqslant 1000$. They observed that the time-averaged drag coefficient decreased as the cylinder aspect ratio was decreased, or as the cylinder became more aerodynamic (less 'bluff'). They further observed that the shedding frequency increased with aspect ratio and Reynolds number. Subsequent investigations were conducted by Kim & Park (2006), where an additional parameter, the angle of incidence of the incoming flow, was considered. They computed the force coefficients and shedding frequencies for an elliptical cylinder for $1.6 \leqslant \Gamma \leqslant 5$, $10 \leqslant I \leqslant 30°$, $400 \leqslant Re \leqslant 600$. They observed that the time-averaged drag coefficient decreased as the aspect ratio was increased and the angle of incidence was decreased, while the lift coefficient increased as the angle of incidence was increased. The Strouhal number was found to decrease as the angle of incidence was decreased. Mittal & Balachandar (1996) performed two- and three-dimensional direct numerical simulations of a flow past an elliptical cylinder for $Re \leqslant 1000$, $I \leqslant 45°$, and observed that the two-dimensional simulations over-predicted the values of the time-mean drag coefficient and the amplitude of lift coefficient obtained from three-dimensional simulations at Reynolds numbers where the flow was intrinsically three-dimensional. For $\Gamma = 2$, $Re = 525$, $I = 0°$, the mean drag coefficient from three-dimensional simulations was in good agreement with its two-dimensional counterpart, and a significant decrease in the amplitude of the lift coefficient was observed after the onset of three-dimensional flow.

Sheard (2007) investigated the three-dimensional stability in the wake of an elliptical cylinder of $\Gamma = 2$ for $I \leqslant 30°$. Unlike the wake transition scenario of a circular cylinder, a new three-dimensional instability, mode $\widehat{\mathrm{B}}$ with a spanwise wavelength of $\lambda/D \simeq 2.4D$, was the first mode to become unstable to perturbations at $Re \simeq 283$. This mode had spatio-temporal characteristics similar to those of the mode B instability and approximately three times its spanwise wavelength. The onset of mode A and mode B instabilities was delayed to values of Reynolds numbers higher than those for a circular cylinder wake. Sheard (2007) further investigated the stability of the flow at $Re = 283.1$ over a range of incident angles, where a long wavelength mode ($\lambda/D \geqslant 6$) was observed for $I \geqslant 15°$, prevalent alongside other shorter wavelength three-dimensional modes with high growth rates. More recently, Leontini *et al.* (2015) presented the parameter map of the three-dimensional instabilities observed for $0 \leqslant \Gamma \leqslant 2.4$ and $Re \leqslant 550$ at zero angle of incidence. In addition to the three-dimensional modes A, B and $\widehat{\mathrm{B}}$ (labelled B^* in Sheard (2007)), they confirmed the presence of the long wavelength mode, mode $\widehat{\mathrm{A}}$, observed in the wake of elongated bluff bodies with elliptical leading edges by Ryan, Thompson & Hourigan (2005) and later by Sheard (2007). Mode $\widehat{\mathrm{B}}$ was found to be unstable for $\Gamma \gtrsim 1.7$. The range of Reynolds number for the existence of mode $\widehat{\mathrm{B}}$ in the $\Gamma - Re$ parameter map increased as the aspect ratio of the elliptical cylinder was increased. The topology of this mode resembled that of a similar wavelength instability observed in the wake of cylinders with an elliptical leading edge (Ryan *et al.* 2005; Thompson

et al. 2006*b*). Mode $\widehat{\mathrm{A}}$ had spatio-temporal characteristics similar to the mode A instability, but was unstable over larger spanwise distances. On closer inspection of the spanwise perturbation contours and the spatio-temporal characteristics, mode $\widehat{\mathrm{A}}$ resembles a longer-wavelength instability previously observed in the wake of a rotating cylinder, mode G (Rao *et al.* 2013*a*, 2015*a*). Mode G was found to be unstable to spanwise perturbations over forty cylinder diameters and occurred at rotation rates $\simeq$1.8. More recently, Kim, Lee & Choi (2016) investigated helically twisted elliptical cylinders of different spanwise wavelengths and aspect ratios at $Re = 100$ and observed a wide range of three-dimensional modes in the wake.

The current systematic study extends the studies of Sheard (2007) and Leontini *et al.* (2015), where Floquet stability analysis is performed for incident angles ($0^\circ \leqslant I \leqslant 20^\circ$) for elliptical cylinders of different aspect ratios $\Gamma \leqslant 4$, $Re \leqslant 500$. Stability analysis is performed to observe the variation of the critical Reynolds numbers for the onset of the three-dimensional modes with incident angles for various aspect ratios, and the nature of how these modes change with control parameters. The remainder of the article is organised as follows; § 2 details the case setup and numerical formulation; § 3 contains the results from the two-dimensional simulations and Floquet stability analysis, and the behaviour of the various three-dimensional modes observed, followed by a few three-dimensional simulations in § 3.10 and conclusions in § 4.

2. Methodology

2.1. *Problem definition*

The schematic of the problem under consideration is shown in figure 1. The aspect ratio of the cylinder (Γ) is defined as the ratio of the major axis (a) to the minor axis (b, D). An aspect ratio of $\Gamma = 0$ corresponds to a flat plate, while $\Gamma = 1$ is equivalent to a circular cylinder. For cases considered here, the aspect ratio was varied between $\Gamma = 1.1$ and 4.0. Rather than rotate the cylinder, for the computations and visualisations presented, the incoming flow is set at an angle of incidence (I) to the major axis of the elliptical cylinder. As indicated, the Reynolds number (Re) is based on the minor axis of the cylinder, time (t) is non-dimensionalised by D/U to give a dimensionless time, $\tau = tD/U$. We investigate the two- and three-dimensional transitions that occur as the Reynolds number is increased up to $Re = 500$. Here, the Reynolds number is based on the minor axis (b) of the cylinder. This choice of length scale seems appropriate for the small angles of incidence considered here. Alternate definitions where the characteristic length is based on the major axis of the ellipse (Griffith *et al.* 2016), geometric mean of the major and minor axis ($(a+b)/2$) or the square root of the product of the major and minor axis ($\sqrt{ab}$) have been used in studies concerning elliptical cylinders rotated along their spanwise length (Jung & Yoon 2014; Kim *et al.* 2016; Wei, Yoon & Jung 2016) and the perimeter of the elliptical cylinder for a rotating elliptical cylinder (Naik, Vengadesan & Prakash 2017). Nonetheless, values can be converted from one system to another as appropriate.

2.2. *Numerical method*

2.2.1. *Flow equations*

The two-dimensional incompressible Navier–Stokes (NS) equations determine the flow fields that the stability analysis is based on

$$\frac{\partial \boldsymbol{u}}{\partial t} + \boldsymbol{u}\cdot\boldsymbol{\nabla}\boldsymbol{u} = -\boldsymbol{\nabla}p + \nu\nabla^2\boldsymbol{u}, \tag{2.1}$$

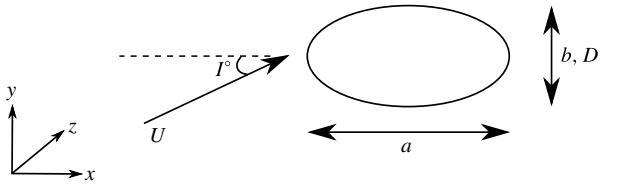

FIGURE 1. Schematic of the elliptical cylinder in a flow at angle of incidence.

where $\boldsymbol{u} = \boldsymbol{u}(x, y; t) = (u(x, y; t), v(x, y; t))$ is the two-dimensional velocity field, p is the kinematic pressure, i.e. the static pressure (P) divided by the fluid density (ρ), and ν is the kinematic viscosity. These equations are coupled with the incompressibility constraint

$$\nabla \cdot \boldsymbol{u} = 0, \tag{2.2}$$

to complete the set of equations governing the flow.

As indicated, to obtain the two-dimensional base flows necessary for the Floquet analysis, these equations are solved numerically. There are two cases of interest for this paper: periodic base flows and steady base flows. For the latter case, the Reynolds number may be above the critical value leading to periodic flow, hence a time-dependent solver cannot be used to obtain these steady flow states. Both cases use a spectral-element formulation with further details provided in Zienkiewicz (1977), Karniadakis & Sherwin (2005), Thompson *et al.* (2006*a*) so only a brief overview of the key elements will be presented here.

The spectral-element method is essentially a high-order finite-element approach but with the internal $N \times N$ nodes within each (spectral) element distributed according to the Gauss–Legendre–Lobatto (GLL) quadrature points. The velocity and pressure fields are represented by tensor products of Lagrangian polynomial interpolants that are constructed using the nodal values within each element. Importantly, the integrals resulting from the application of the Galerkin weighted-residual method to the NS equations, which contribute to form the discrete approximation at each node point (e.g. Karniadakis & Sherwin 2005), are evaluated by GLL quadrature. This method achieves spectral convergence as the polynomial order is increased within elements (Karniadakis & Sherwin 2005). For the simulations reported in this paper, the computational domain consisted of several hundred four-sided macro-elements, with higher concentration in the vicinity of the elliptic cylinder where the velocity gradients were largest. The curvature of element sides forming the boundary of the cylinder is taken into account by mapping each element in (x, y) physical space to a square in (ξ, ζ) computational space, as is common with the finite-element approach (Zienkiewicz 1977; Karniadakis & Sherwin 2005). Importantly, the number of node points within each element ($N \times N$) is specified at runtime, with the interpolating polynomial order in each direction being $N - 1$. At the very least, this tends to simplify convergence studies.

A second-order fractional time stepping technique is used to sequentially integrate the advection, pressure and diffusion terms of the Navier–Stokes equations forward in time (see, e.g., Chorin 1968; Karniadakis, Israeli & Orszag 1991; Thompson *et al.* 2006*a*). A third-order Adams–Bashforth method is used for the advection substep, together with a θ-modified Crank–Nicholson method (e.g. Canuto *et al.* 1988) for the diffusion step. The incompressibility constraint is applied at the end of the second substep to enforce mass conservation from one time step to the next.

Formally, the method is second-order accurate in time by applying a higher-order pressure boundary condition at solid surfaces, as discussed in Karniadakis *et al.* (1991). Both the pressure and viscous substeps are implicit. The resulting sparse matrix equations are inverted using lower–upper decomposition, so that for each time step, subsequent substep updates only require matrix–vector multiples.

The unsteady solver was used to compute the base flows to investigate the parameter range covering both the steady and unsteady regimes of flow. More details of the time stepping scheme can be found in Thompson *et al.* (2006*a*), Leontini *et al.* (2015) and the references therein, and the code has previously been used to accurately compute bluff body flows in free stream (Sheard *et al.* 2004*b*; Ryan *et al.* 2005; Leontini *et al.* 2007; Rao *et al.* 2013*a*; Thompson *et al.* 2014; Leontini *et al.* 2015), and for bodies near walls (Stewart *et al.* 2006, 2010; Rao *et al.* 2011, 2012, 2013*c*). In order to achieve steady base flows for standard linear stability analysis based on steady flow fields at parameter values that would normally result in a periodic flow (see § 2.8), the steady incompressible NS equations were solved incorporating the incompressibility constraint into the NS equations using the penalty method (Zienkiewicz 1977), which eliminates direct reference to the pressure field. The resulting nonlinear coupled discretised equations for the velocity components at the node points were then solved using Newton iteration (Thompson & Hourigan 2003; Jones, Hourigan & Thompson 2015; Rao, Thompson & Hourigan 2016).

2.2.2. *Stability analysis*

To determine the stability of the calculated two-dimensional periodic or steady base flows, which are now referred to using an overbar, the velocity and pressure fields are expanded about the base states: $\boldsymbol{u}(x, y, z; t) = \overline{\boldsymbol{u}}(x, y; t) + \boldsymbol{u}'(x, y, z; t)$, $p(x, y, z; t) = \overline{p}(x, y; t) + p'(x, y, z; t)$. Substituting these expansions into the NS equations, subtracting off the NS equations for the base flow and neglecting nonlinear terms gives

$$\frac{\partial \boldsymbol{u}'}{\partial t} + \overline{\boldsymbol{u}} \cdot \boldsymbol{\nabla} \boldsymbol{u}' + \boldsymbol{u}' \cdot \boldsymbol{\nabla} \overline{\boldsymbol{u}} = -\boldsymbol{\nabla} p' + \nu \boldsymbol{\nabla}^2 \boldsymbol{u}' \quad \text{and} \quad \boldsymbol{\nabla} \cdot \boldsymbol{u}' = 0. \tag{2.3a,b}$$

Since these equations are linear with constant coefficients with respect to the spanwise coordinate z, the spatial dependence can be written as a sum of complex exponentials. In fact, in this case, simple sine and cosine expansions are sufficient (Barkley & Henderson 1996). That is, take

$$\left.\begin{aligned} u' &= \sum_{k=0}^{M} \hat{u}(x, y; t) \cos(2\pi k z / L_z), \quad & v' &= \sum_{k=0}^{M} \hat{v}(x, y; t) \cos(2\pi k z / L_z), \\ w' &= \sum_{k=0}^{M} \hat{w}(x, y; t) \sin(2\pi k z / L_z), \quad & p' &= \sum_{k=0}^{M} \hat{p}(x, y; t) \cos(2\pi k z / L_z), \end{aligned}\right\} \tag{2.4}$$

where L_z is the length of the chosen spanwise domain, with periodicity assumed at each end and where M is the number of Fourier modes. Putting in these expansions into (2.3), gives the following equations for each spanwise mode number k

$$\frac{\partial \hat{u}}{\partial t} + \overline{\boldsymbol{u}} \cdot \boldsymbol{\nabla}_{xy} \hat{u} + \hat{\boldsymbol{u}} \cdot \boldsymbol{\nabla}_{xy} \overline{u} = -\frac{\partial \hat{p}}{\partial x} + \nu \nabla_{xy}^2 \hat{u} - \left(\frac{2\pi k}{L_z}\right)^2 \hat{u}, \tag{2.5}$$

$$\frac{\partial \hat{v}}{\partial t} + \overline{\boldsymbol{u}} \cdot \boldsymbol{\nabla}_{xy} \hat{v} + \hat{\boldsymbol{u}} \cdot \boldsymbol{\nabla}_{xy} \overline{v} = -\frac{\partial \hat{p}}{\partial y} + \nu \nabla_{xy}^2 \hat{v} - \left(\frac{2\pi k}{L_z}\right)^2 \hat{v}, \tag{2.6}$$

$$\frac{\partial \hat{w}}{\partial t} + \overline{\boldsymbol{u}} \cdot \boldsymbol{\nabla}_{xy} \hat{w} = \frac{2\pi k}{L_z} \hat{p} + \nu \nabla_{xy}^2 \hat{w} - \left(\frac{2\pi k}{L_z}\right)^2 \hat{w}, \tag{2.7}$$

$$\frac{\partial \hat{u}}{\partial x} + \frac{\partial \hat{v}}{\partial y} + \frac{2\pi k}{L_z} \hat{w} = 0. \tag{2.8}$$

Here, the vector derivative operators are two-dimensional, i.e.

$$\nabla_{xy}^2 \equiv \partial^2/\partial x^2 + \partial^2/\partial y^2, \quad \boldsymbol{\nabla}_{xy} \equiv \boldsymbol{i}\partial/\partial x + \boldsymbol{j}\partial/\partial y, \tag{2.9a,b}$$

with $\boldsymbol{i}$, $\boldsymbol{j}$ the x and y Cartesian unit vectors.

This is essentially an eigenvalue problem for each of the mode coefficient fields (e.g. $\hat{u}_k(x, y; t)$) noting that because of linearity in time, the time variation will be (possibly complex) exponential. The solutions of interest are the fast-growing or slowest-decaying ones. These can be obtained by integrating these equations forward in time starting from an initially random field, until the fastest-growing/slowest-decaying modes dominate. Because the equations are of the same form as the NS equations for the base flow, the same solution technique is applied. In practice, the base flow solutions are found first by integrating forward in time for 50–80 base flow periods and then the stability equations for a chosen spanwise wavelength ($\lambda = L_z/k$) are integrated forward in time together with the base flow equations to determine the dominant instability modes. The parallel version of the code computes the solution for multiple wavelengths simultaneously, so that the simultaneous integration of the base flow equations only adds trivially to the overall cost.

After a few tens of periods (typically 10–50), the fastest-growing modes dominate. For a periodic base flow, the amplification of these dominant modes is determined over each base flow period; this technique is known as Floquet analysis. If the base flow is steady, it is convenient to measure the growth rate over a unit time. In both cases, the stability multiplier (μ), measures the amplification rate of the perturbations over the chosen time interval (T). This is called the Floquet multiplier for the periodic base flow case. In either case, the growth rate (σ) is determined by $\sigma = \log_e(\mu)/T$. For growth rates greater than 0 (or $|\mu| > 1$), the flow is unstable to three-dimensional perturbations at the chosen wavelength and for $\sigma < 0$ (or $|\mu| < 1$), perturbations decay and the flow remains in its two-dimensional state. For $\sigma = 0$ (or $|\mu| = 1$), neutral stability is achieved. For a given Reynolds number, a range of spanwise wavelengths is tested, and this procedure is repeated for a range of Reynolds numbers to determine the critical Reynolds number and wavelength at which neutral stability is achieved. For the transition from two-dimensional steady to two-dimensional periodic flow, the method can also be applied by considering a spanwise wavelength approaching infinity. The complex growth rate or multiplier then gives the growth rate and frequency of the unstable oscillatory mode. Modes other than just the dominant mode have been extracted in this study using a Krylov subspace approach together with Arnoldi decomposition (see, e.g., Mamun & Tuckerman 1995; Barkley & Henderson 1996).

For periodic base flows, three-dimensional modes that have a positive and a purely real multiplier are referred to as synchronous modes (i.e. the period of the Floquet mode matches that of the two-dimensional base flow, such as modes A and B), while those that have a negative and purely real multiplier real component are known as subharmonic modes or period-doubling modes (such as mode C). Quasi-periodic (QP) modes have a complex-conjugate multiplier pair and are usually observed at Reynolds numbers past the transition of modes A and B in wake flows. When represented on a complex plane, the synchronous multipliers lie on the positive real

axis, the subharmonic modes lie on the negative real axis. Quasi-periodic modes have a reflection symmetry about the real axis with a non-zero imaginary component (Blackburn *et al.* 2005; Blackburn & Sheard 2010). More details on the stability analysis employed in this study can be found in Ryan *et al.* (2005), Griffith *et al.* (2007), Leontini *et al.* (2015) and Rao *et al.* (2015*a*).

2.2.3. *Three-dimensional simulations*

In addition to the stability analysis, some full three-dimensional simulations were undertaken to examine the nonlinear evolution of the flow. These simulations used a version of the spectral-element code extended to three dimensions by representing the z dependence of the flow variables by Fourier expansions. In this case, the advection substep is performed in real space and the pressure and diffusion substeps in Fourier space. The latter allows a natural parallelisation by treating each Fourier mode independently on different central processing unit (CPU) cores, while parallelisation of the advection substep proceeds by distributing computations to discrete sets of nodes. Full details of the method are provided in Karniadakis & Triantafyllou (1992).

3. Results

3.1. *Spatial and domain size studies*

The parameter space maps for different aspect ratios investigated in this study are presented for $Re \leqslant 500$. The aspect ratios chosen for the stability analysis in this study were $\Gamma = 1.1$, 1.5, 2 and 2.5 for angles of incidence less than 20°.

The domain size chosen for this study had the inlet and lateral boundaries $60D$ away from the cylinder and the outlet placed at $100D$ downstream of the cylinder to minimise blockage effects. The blockage ratio was less than 1 %. Furthermore, domain size studies were conducted with inlet, lateral and outlet boundaries at $60D$, $100D$ and $200D$ from the cylinder. The force coefficients, and shedding frequencies for the domain chosen were well within 0.5 % (e.g. $\Delta C_D = 0.25\,\%$, $\Delta C_{L,RMS} = 0.5\,\%$, $\Delta St = 0.14\,\%$, for $\Gamma = 2$, $I = 0°$, $Re = 440$) of the largest domain. Furthermore, spatial resolution studies were conducted for aspect ratios of 1.1, 1.5, 2 and 2.5 at incident angles of 0°, 10° and 20° and Reynolds number of 500 by varying the polynomial order of the spectral elements from $N = 4$ to $N = 11$. For $N = 8$, the force coefficients and the shedding frequencies for the cases were well within 1 % (e.g. $\Delta C_D = 0.01\,\%$, $\Delta C_{L,RMS} = 0.6\,\%$, $\Delta St = 0.02\,\%$, for $\Gamma = 2.5$, $I = 0°$, $Re = 500$) of the maximum polynomial order. Additionally, a time step resolution study undertaken showed that the variation in the force coefficients and shedding frequencies were again within 1 % of the values for the minimum time step used. A further validation of the results was the good agreement with the critical Reynolds number for the onset of unsteady flow by Jackson (1987) and the Floquet multipliers presented for $\Gamma = 2$, $I = 0°$, $Re = 400$ by Sheard (2007). As an indicator of convergence for the Floquet analysis for a typical case, the difference between the computed Floquet multiplier using 8×8 and 10×10 nodes per element was less than 0.01 % for mode QPA at $\Gamma = 2.5$, $I = 16°$, $Re = 260$, $\lambda/D = 3.9$. The domain size study and spatial resolution studies are documented in appendices A and B, respectively.

3.2. *Two-dimensional flow*

As the Reynolds number is increased beyond the onset of unsteady flow, periodic shedding similar to BvK shedding is observed. For a given aspect ratio and incident

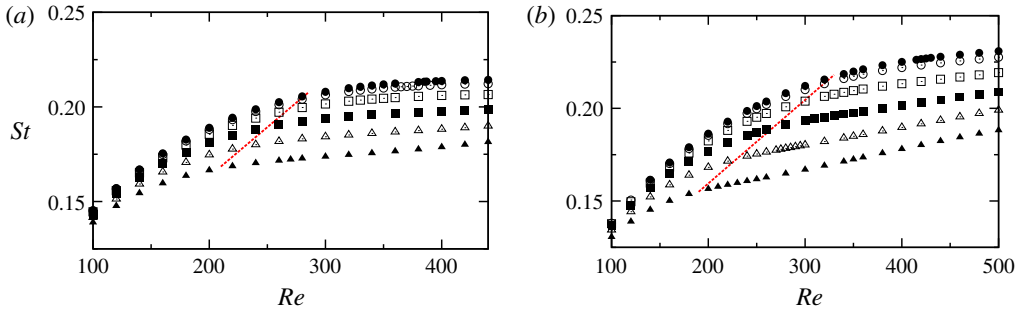

FIGURE 2. (Colour online) Variation of the Strouhal number, St, versus Reynolds number, Re, for (*a*) $\Gamma = 2$ and (*b*) $\Gamma = 2.5$, for various incident angles of: $I = 0°$ (●), $I = 4°$ (○), $I = 8°$ (□), $I = 12°$ (■), $I = 16°$ (△) and $I = 20°$ (▲). The shedding frequency decreases with an increase in the angle of incidence. The dashed red line approximately marks the critical Reynolds number for the transition to three-dimensional flow.

angle, the Strouhal number ($St = fD/U$, where f is the frequency of vortex shedding (Strouhal 1878)), is observed to increase monotonically with Reynolds number. However, as the angle of incidence is varied from $I = 0°$ to 20°, St decreases with an increase in incident angle. Shown in figure 2 is the St variation with the angle of incidence for $\Gamma = 2$ and 2.5. Also marked on these plots by a dashed red line is the approximate Reynolds number for the onset of three-dimensional flow. Beyond this critical value, St varies almost linearly with Re.

The variation of the critical Reynolds number for the onset of unsteady flow is shown in the parameter space maps of the aspect ratios investigated here. The onset of unsteady flow occurs at lower Reynolds number as the incident angle is increased, as observed by Paul, Prakash & Vengadesan (2014*b*). The critical values obtained at low angles of incidence are within the 15 % error tolerance of their functional relationship. Furthermore, Paul, Prakash & Vengadesan (2014*a*) have provided functional fits for time-averaged lift and drag coefficients for elliptical cylinders for $Re \leqslant 200$.

3.3. *Transition to three-dimensional flow*

The $Re - I$ parameter space maps of the marginal stability curves for the onset of unsteady flow and three-dimensional modes for $\Gamma = 1.1$, 1.5, 2 and 2.5 are shown in figures 3–5 and 7, respectively. For $\Gamma = 1.1$, the three-dimensional transition scenario is similar to that of a circular cylinder. With increasing Reynolds number, the base flow is first unstable to mode A, then mode B, then mode QP. The angle of incidence only has a marginal effect. As the aspect ratio of the cylinder is increased, the complexity of these parameter space maps increases, with modes $\widehat{\text{A}}$ and C being observed for $\Gamma \geqslant 1.5$ and modes $\widehat{\text{B}}$ and QPA being observed for $\Gamma \gtrsim 1.8$, in addition to modes A, B and QP. (A description of these different modes is given in later sections.) The panels in each of these parameter space plots show the regions of occurrence of these three-dimensional modes. The region of each mode is assigned a unique colour and these coloured regions are overlaid to produce the parameter space maps. The reader is also referred to Leontini *et al.* (2015) for the various transitions that occur the wake of an elliptical cylinder at zero incident angle.

Shown in figure 3 are the marginal stability curves for $\Gamma = 1.1$. At lower angles of incidence, the critical values of transition are similar to those of a cylinder of

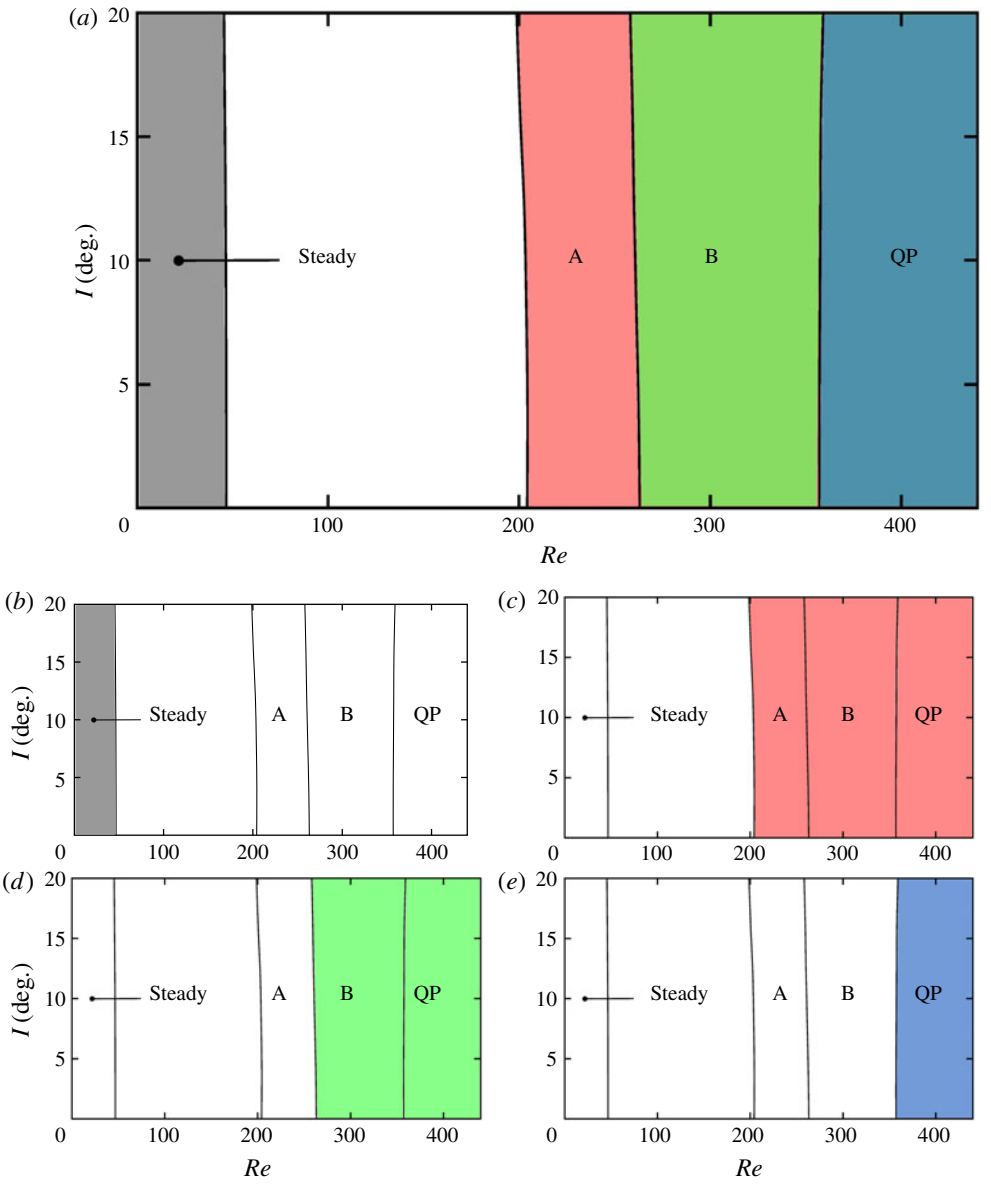

FIGURE 3. (Colour online) (*a*) Marginal stability diagram of the $Re - I$ parameter space showing the various transitions for $Re \leqslant 440, I \leqslant 20°$ for the elliptical cylinder of $\Gamma = 1.1$. (*b*) Regions of steady flow and three-dimensional instabilities – (*c*) mode A, (*d*) mode B and (*e*) mode QP are each assigned a unique colour and overlaying these regions gives the composite image in (*a*).

$\Gamma = 1$, and vary only slightly as the incident angle is increased up to $I = 20°$. While the critical Reynolds number (Re_c) for the onset of modes A and B decreases marginally as the incident angle is increased, Re_c marginally increases for mode QP. The preferred spanwise wavelengths of these modes at onset remain relatively constant over this incident angle range.

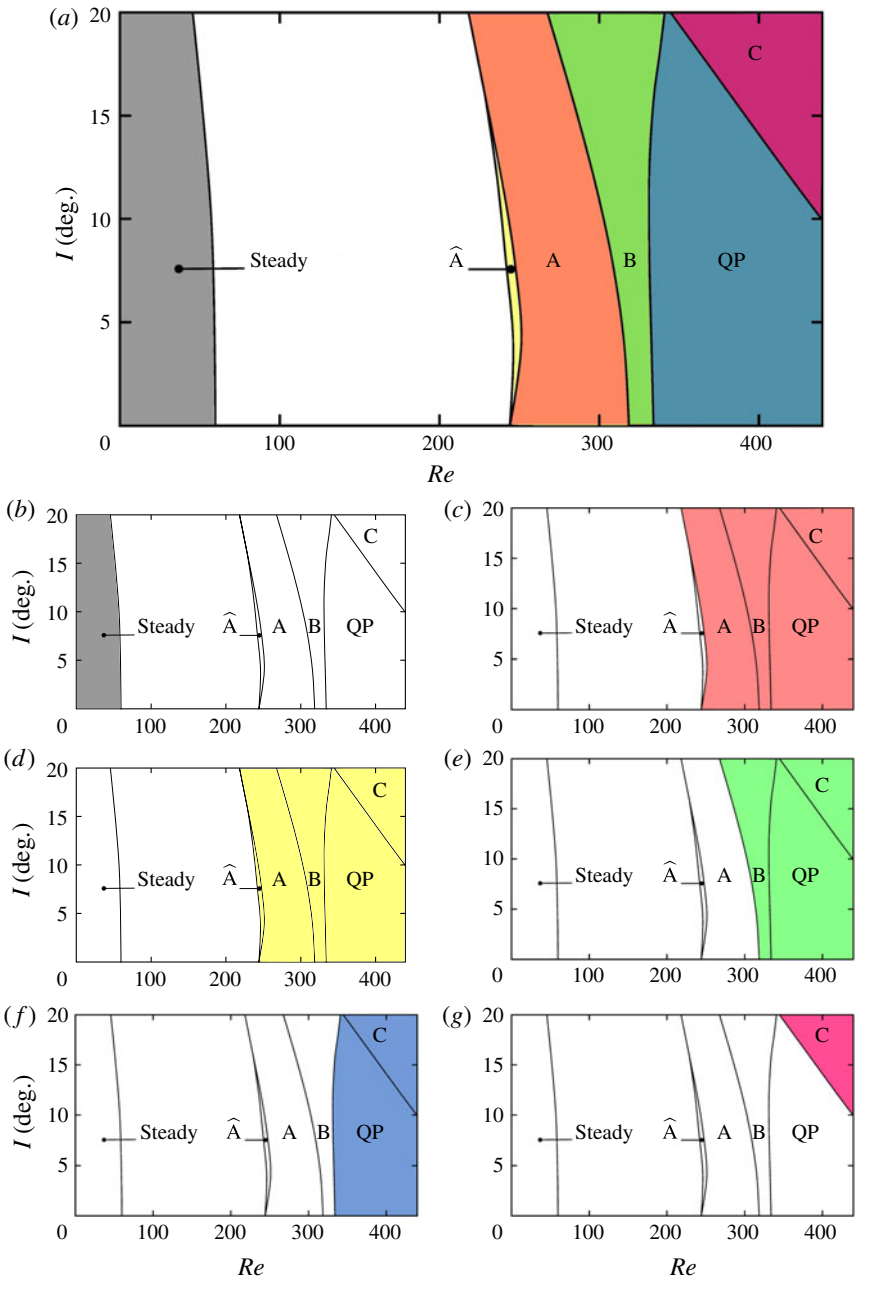

FIGURE 4. (Colour online) (*a*) Marginal stability diagram of the $Re - I$ parameter space showing the various transitions for $Re \leqslant 440, I \leqslant 20°$ for the elliptical cylinder of $\Gamma = 1.5$. (*b*) Regions of steady flow and three-dimensional instabilities: (*c*) mode A, (*d*) mode $\widehat{\text{A}}$, (*e*) mode B, (*f*) mode QP and (*g*) mode C are each assigned a unique colour and overlaying these regions gives the composite image in (*a*).

Figure 4 shows the parameter space map for an aspect ratio $\Gamma = 1.5$. Leontini *et al.* (2015) reported the onset of a long wavelength mode, mode $\widehat{\text{A}}$, to become

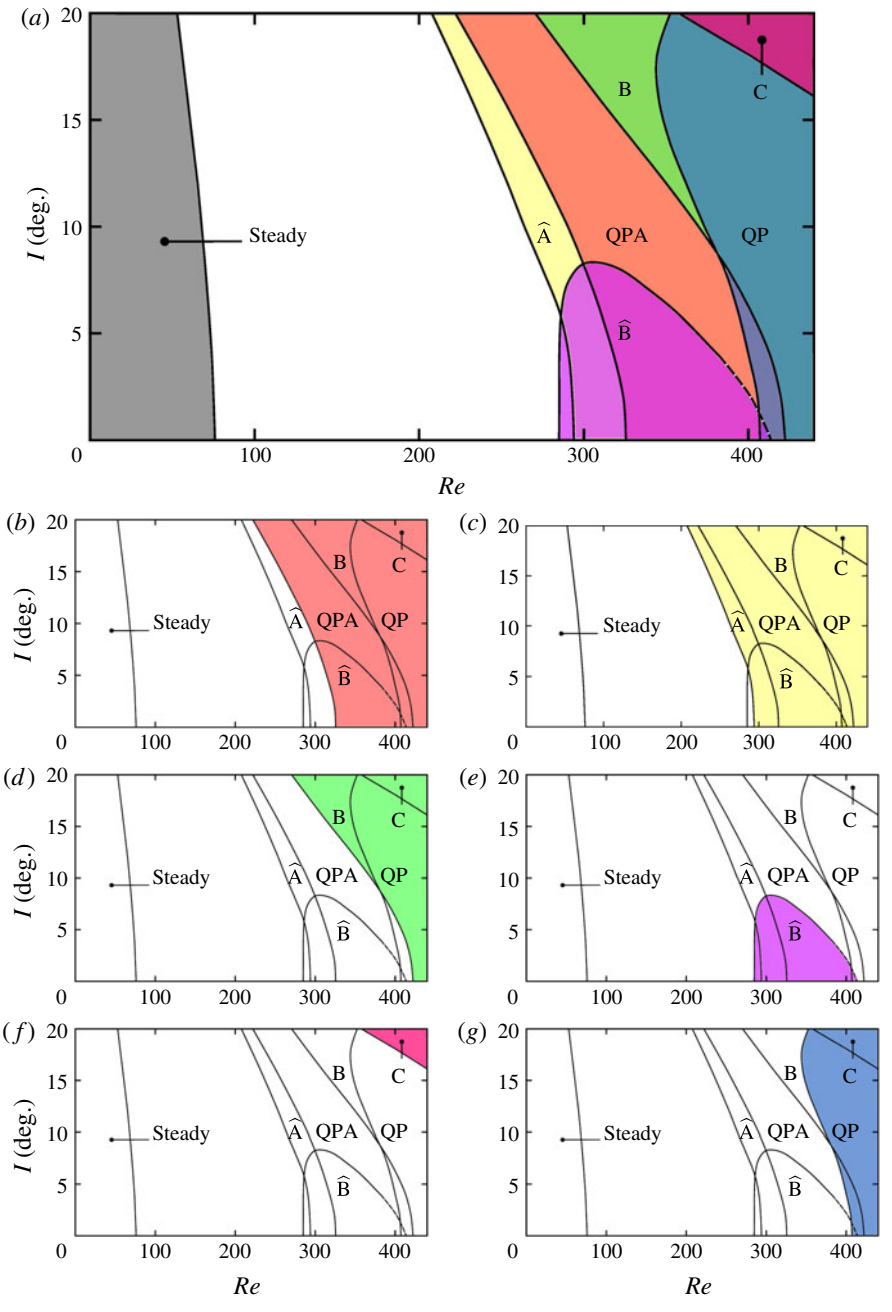

FIGURE 5. (Colour online) (*a*) Marginal stability diagram of the $Re - I$ parameter space showing the various transitions for $Re \leqslant 440$, $I \leqslant 20°$ for the elliptical cylinder of $\Gamma = 2$. Regions of three-dimensional instabilities – (*b*) mode QPA, (*c*) mode $\widehat{\mathrm{A}}$, (*d*) mode B, (*e*) mode $\widehat{\mathrm{B}}$, (*f*) mode C and (*g*) mode QP are each assigned a unique colour and overlaying these regions gives the composite image in (*a*). The dashed line of mode $\widehat{\mathrm{B}}$ indicates the extrapolated values at lower angles of incidence.

unstable for $\Gamma \gtrsim 1.2$ at $I = 0°$, and this mode is observed to occur at Reynolds numbers close to the onset of mode A for $\Gamma = 1.5$. The boundaries of the these two modes are contiguous in the $Re - I$ space. Modes A and $\widehat{\text{A}}$ appear as two separate branches at lower Reynolds numbers; the two modes coalesce at higher Reynolds numbers (Leontini *et al.* 2015). As the incident angle is increased for this aspect ratio, the onset of modes $\widehat{\text{A}}$ and B decreases to lower Reynolds numbers, while that of mode A increases marginally as the incident angle is first increased from $I = 0°$ to $I = 4°$, before decreasing to lower values as the incident angle is increased further. However, the onset of mode QP is delayed to higher Reynolds numbers with increasing angle of incidence. For $I \gtrsim 12°$, mode C is observed at the upper range of Reynolds numbers investigated here, and the critical Reynolds number for the onset of mode C decreases to lower Reynolds numbers as the angle of incidence is increased, with a marginal increase in the spanwise wavelength. Mode C is observed to become unstable at the lower range of wavelengths of the unstable mode QP. At lower incident angles of $I \simeq 12°$, the onset of mode C occurs well past the Re_c for mode QP; however, at higher incident angles ($I \simeq 20°$), the critical Reynolds number for the onset of mode C occurs close to the onset of mode QP.

Figure 5 shows the marginal stability curves for $\Gamma = 2$. Mode $\widehat{\text{B}}$ is the first three-dimensional mode to become unstable to perturbations at low angles of incidence and forms a closed region in the parameter space, occurring for $I \leqslant 9°, 285 \lesssim Re \lesssim 420$. At Reynolds numbers past the onset of modes $\widehat{\text{B}}$ and $\widehat{\text{A}}$, mode QPA is observed. For incident angles $I \gtrsim 2°$, this mode manifests as a quasi-periodic instability, whose imaginary component of the Floquet multiplier increases with an increase in the incident angle. Also, for a given incident angle, the imaginary component of the mode decreases with increasing Reynolds number and a real mode whose structure resembles mode A is observed. This mode is discussed in detail in § 3.5 with respect to $\Gamma = 2.5$. The onset of mode B occurs at decreasing Reynolds numbers with increasing angles of incidence. However, the onset of mode QP occurs at lower Reynolds numbers as angle of incidence is increased from 0° and increases to higher Reynolds numbers beyond $I = 15°$. At higher Reynolds numbers, mode C becomes unstable for $I \gtrsim 18°$ (also see § 3.8). Comparing figures 4 and 5, the angle of incidence for the onset of mode C increases to higher values as the aspect ratio is increased from $\Gamma = 1.5$ to 2.

Figure 6 shows spanwise perturbation vorticity contours for an elliptical cylinder at $\Gamma = 2$ at the specified parameter values for the various three-dimensional modes observed in this study. These images bear a resemblance to the vorticity contours shown in figure 2 of Leontini *et al.* (2015), albeit rotated due to the incoming flow at an incident angle and also to the vorticity contours of the corresponding modes observed in the wake of a rotating circular cylinder at low rotation rates (Rao *et al.* 2013*a*, 2015*a*). The physical mechanisms and the spatio-temporal characteristics of these modes have been previously detailed by Leontini *et al.* (2015) and earlier works. The perturbation vorticity contours of modes A (also, mode QPA) and mode $\widehat{\text{A}}$ at onset appear to be similar in the near wake but differ in the shed vortices further downstream of the body (Leontini *et al.* 2015). Closer examination of the perturbation contours of mode $\widehat{\text{A}}$ reveals that it is mode G, which was observed in the wake of rotating cylinders. Mode $\widehat{\text{A}}$ and mode G share the same spatio-temporal characteristics and have wavelengths of the order of several tens of diameters in the spanwise direction (also see figure 23 of Rao *et al.* (2013*a*)). This is detailed in § 3.6, where the relationship of mode A and $\widehat{\text{A}}$ are discussed. The perturbation contours of

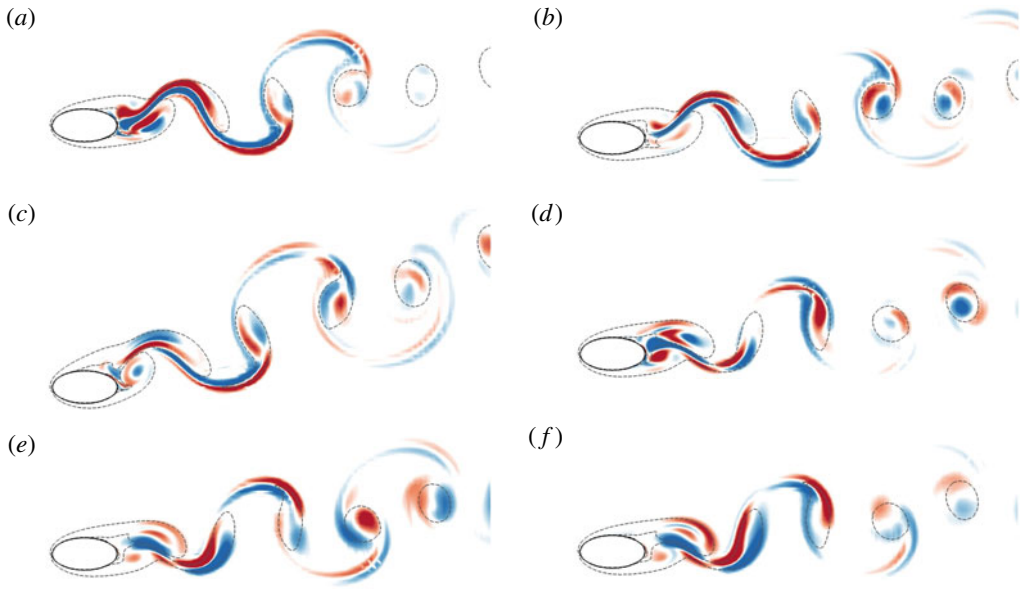

FIGURE 6. (Colour online) Visualisation of spanwise perturbation vorticity contours for $\Gamma = 2$ at the specified parameter values, and in the increasing order of their characteristic spanwise wavelengths, for (*a*) mode B: $Re = 400$, $\lambda/D = 0.85$, (*b*) mode QP: $Re = 400$, $\lambda/D = 1.9$, (*c*) mode C: $I = 20°$, $Re = 360$, $\lambda/D = 2.1$, (*d*) mode $\widehat{\text{B}}$: $Re = 320$, $\lambda/D = 2.5$, (*e*) mode QPA: $Re = 320$, $\lambda/D = 4$ and (*f*) mode $\widehat{\text{A}}$: $Re = 320$, $\lambda/D = 8$. Spanwise perturbation vorticity contour levels are between $\pm 0.1D/U$ and are overlaid by dashed lines (——) that indicate the base flow vorticity contour levels between $\pm 1D/U$. Modes QPA, $\widehat{\text{A}}$ and $\widehat{\text{B}}$ have been captured at the same instant of vortex shedding at $I = 8°$, $Re = 320$; modes B and QP have been captured at the same instant of vortex shedding at $I = 8°$, $Re = 400$; mode C has been captured at $I = 20°$, $Re = 360$. Flow is from left to right in all images.

mode C, has been shown at $I = 20°$ as it appears at larger values of incident angles due to the wake asymmetry; as previously observed in the wakes of rotating cylinders (Rao *et al.* 2013*a*, 2015*a*; Radi *et al.* 2013) and inclined square cylinders (Sheard *et al.* 2009; Sheard 2011).

The parameter space diagram for $\Gamma = 2.5$ is presented in figure 7 showing the various three-dimensional modes that occur for $Re \leqslant 500$. As the angle of incidence is increased, the critical Reynolds number for the onset of unsteady flow decreases from $Re \simeq 93.5$ at $I = 0°$ to $Re \simeq 52$ at $I = 20°$. At low angles of incidence, mode $\widehat{\text{B}}$ is the first three-dimensional mode to become unstable to spanwise perturbations; however, as the angle of incidence is increased beyond $I = 8°$, mode $\widehat{\text{A}}$ becomes the first three-dimensional mode to become unstable. Mode $\widehat{\text{B}}$ is unstable over a larger region of the parameter space as compared to the previous case at $\Gamma = 2$. While mode C was observed only at higher incident angles at aspect ratios of $\Gamma = 1.5$ and 2, a closed region of mode C is observed here for $5° \lesssim I \lesssim 12°$ for $340 \leqslant Re \leqslant 480$. The perturbation structure of mode C at this aspect ratio is very similar to that shown in figure 6, although the critical spanwise wavelength at onset is $\simeq 1.1D$. At Reynolds numbers past the onset of modes $\widehat{\text{A}}$ (and mode $\widehat{\text{B}}$ at lower incident angles), mode QPA

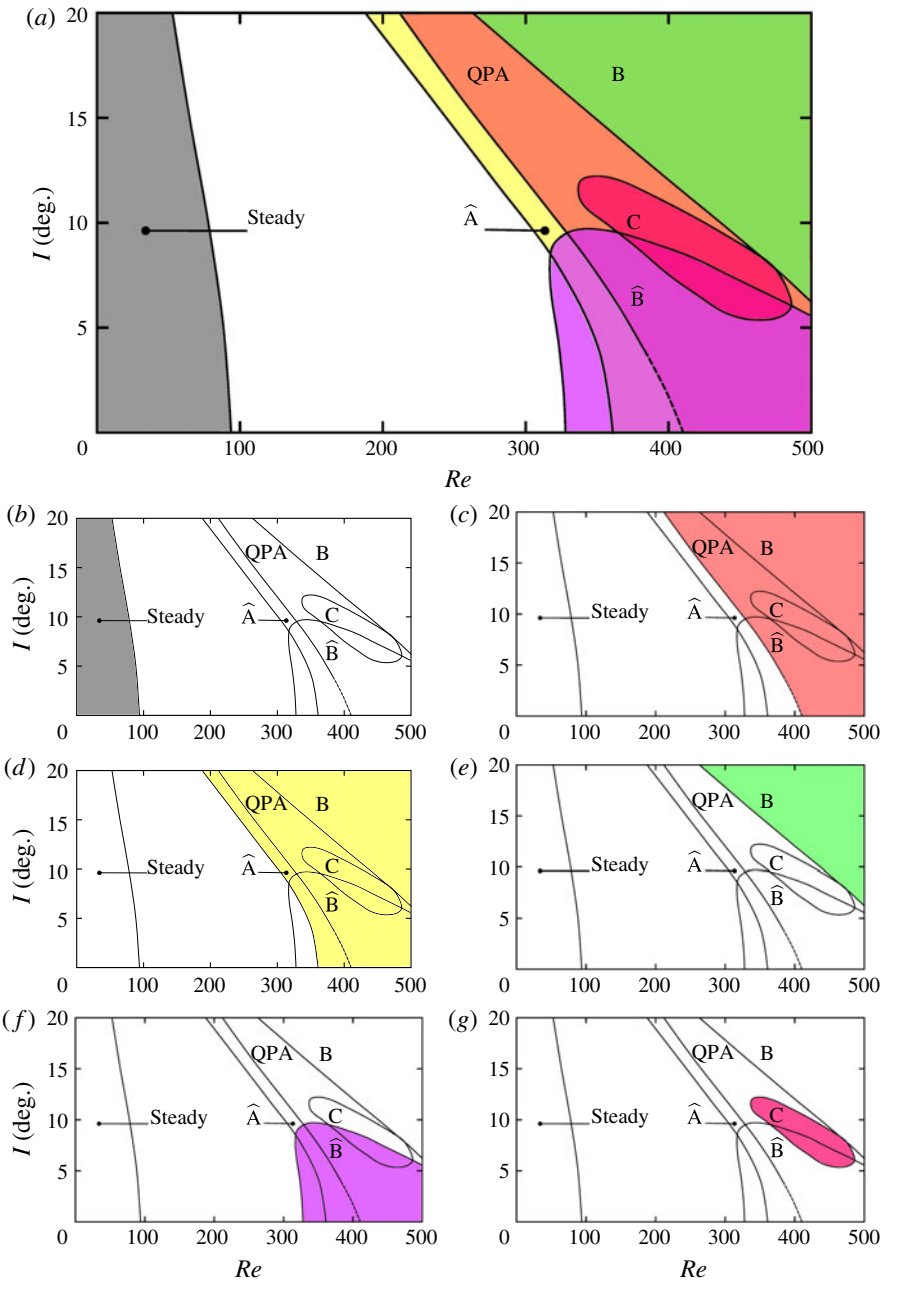

FIGURE 7. (Colour online) (*a*) Marginal stability diagram of the $Re - I$ parameter space showing the various transitions for $Re \leqslant 500, I \leqslant 20°$ for the elliptical cylinder of $\Gamma = 2.5$. (*b*) Regions of steady flow and three-dimensional instabilities: (*c*) mode QPA, (*d*) mode $\widehat{\mathrm{A}}$, (*e*) mode B, (*f*) mode $\widehat{\mathrm{B}}$ and (*g*) mode C are each assigned a unique colour and overlaying these regions gives the composite image in (*a*).

is observed. At lower incident angles, the critical Reynolds number for the onset of mode QPA is more difficult to determine, as the spanwise wavelength at which this

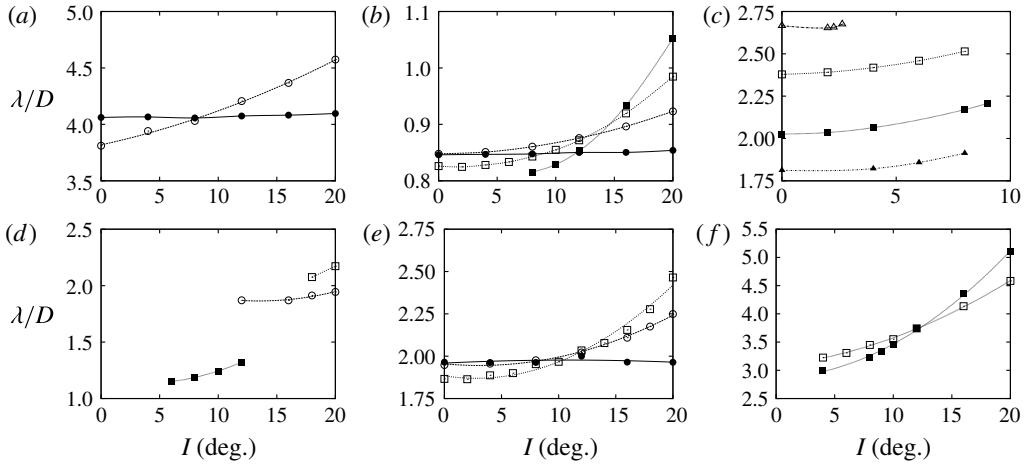

FIGURE 8. Variation of the critical spanwise wavelength at onset for $Re \leqslant 500$ for (*a*) mode A, (*b*) mode B, (*c*) mode $\widehat{\mathrm{B}}$, (*d*) mode C, (*e*) mode QP and (*f*) mode QPA. The aspect ratios are assigned a specific symbol and line type; $\Gamma = 1.1$ (●), $\Gamma = 1.5$ (○), $\Gamma = 1.8$ (△), $\Gamma = 2$ (□), $\Gamma = 2.5$ (■) and $\Gamma = 3$ (▲).

mode occurs is in the same range of wavelengths where mode $\widehat{\mathrm{B}}$ is unstable. Hence, this region is marked by dashed lines in figure 7. At large values of incident angle and Reynolds numbers, modes A and B were the fastest growing modes. A stable quasi-periodic mode of with a dominant wavelength of $\lambda/D = 1.6$ was observed at $I = 20°$, $Re = 500$.

3.4. *Variation of the critical spanwise wavelength*

The variation of the critical spanwise wavelength (λ_c/D) of the three-dimensional modes on the unsteady flow with angle of incidence is shown in figure 8. At low aspect ratios, the variation of the critical wavelength with incident angle is nearly constant and at higher aspect ratios, this variation is marked. The critical wavelengths at $I = 0°$ of modes A, B, $\widehat{\mathrm{B}}$ and QP decrease with an increase in the aspect ratio, as observed in Leontini *et al.* (2015). The critical spanwise wavelengths for mode $\widehat{\mathrm{B}}$ and mode C for $\Gamma = 2.5$ were obtained at the lowest Reynolds number at which this mode is observed to become unstable to perturbations. The variation of the spanwise wavelength with Reynolds number and incident angle for mode $\widehat{\mathrm{B}}$ and mode C is discussed in §§ 3.7 and 3.8, respectively. The variation of the spanwise wavelength of mode $\widehat{\mathrm{A}}$ has not been documented due to peak growth rates occurring at increasingly lower spanwise wavelengths with small increments in Reynolds numbers beyond the critical value of transition. At higher Reynolds numbers, there is no distinct peak for the mode $\widehat{\mathrm{A}}$ curve, as mode A and $\widehat{\mathrm{A}}$ merge (Leontini *et al.* 2015). This is also discussed in § 3.6. At Reynolds numbers past the transitional values, there is a possibility of the interaction of these modes, and thus, the spanwise wavelength observed in reality could be significantly altered.

3.5. *Nature of mode QPA*

For $\Gamma \gtrsim 1.8$, at incident angles $I \gtrsim 2°$, a quasi-periodic mode, mode QPA, becomes unstable to perturbations at Reynolds numbers beyond the onset of mode $\widehat{\mathrm{A}}$.

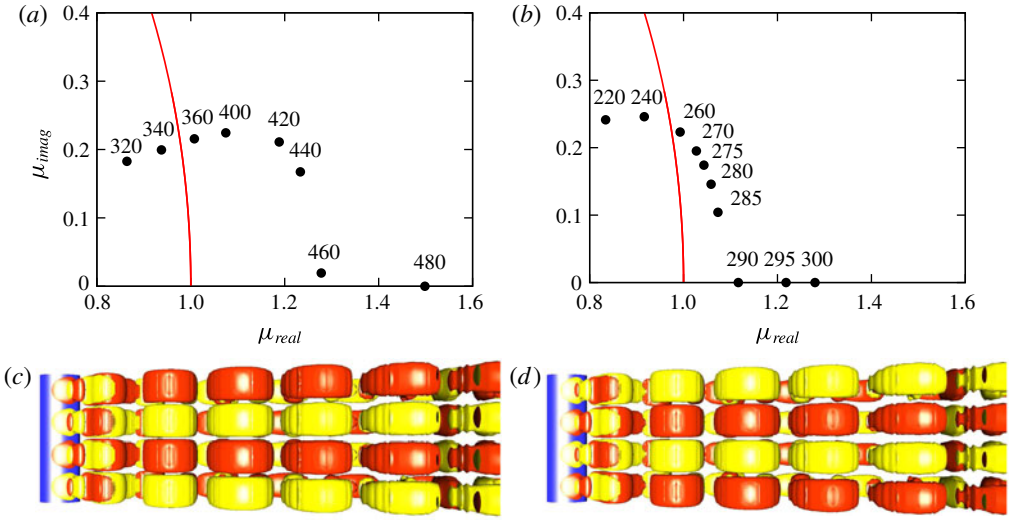

FIGURE 9. (Colour online) Locus of the Floquet multipliers on the complex plane at the specified Reynolds numbers at $\Gamma = 2.5$ at (*a*) $I = 8°$ for a spanwise wavelength of $\lambda/D = 3.6$ and (*b*) $I = 16°$ for a spanwise wavelength of $\lambda/D = 4.5$. The unit circle ($|\mu| = 1$) is shown by the curved red line. For clarity, only the positive component of the complex-conjugate pair of the multipliers is shown in these figures. Three-dimensional reconstructions of mode QPA in plan view taken at (*c*) $t = t_o$ and (*d*) $t = t_o + 17T_{2D}$ at $\Gamma = 2.5$, $I = 8°$, $Re = 400$ showing two spanwise wavelengths of the instability over a spanwise distance of $8D$. Isosurfaces of streamwise perturbation vorticity (in red and yellow) are visualised with the cylinder (in blue). Flow is from left to right in images (*c*,*d*).

This mode has a complex valued Floquet multiplier when $\mu < 1$ (or $\sigma < 0$). On increasing the Reynolds number, the imaginary component of this quasi-periodic mode gradually decreases to zero, and thereby becomes a real synchronous mode. This is similar to the quasi-periodic mode found in the wake of a square cylinder, where the imaginary component of the Floquet multiplier decreases with an increase in Reynolds number (see figure 4 of Blackburn & Lopez (2003)). Similar quasi-periodic modes (QP and QP2) have been reported in the wakes of flat plates and low aspect ratio rectangular cylinders at zero incident angles (Choi & Yang 2014). In these cases, the QP modes do not transform into a real mode because of symmetry restrictions, unlike the case here, where centreline symmetry is broken for non-zero incidence. Perhaps surprising is that mode QPA appears to be a modulated mode A instability, having similar perturbation structure and spanwise wavelength at onset.

Shown in figure 9(*a*,*b*) are the loci of the Floquet multipliers of mode QPA on the complex plane for the elliptical cylinder $\Gamma = 2.5$ at $I = 8°$ and 16°, respectively, at a constant wavelength. For clarity, only the positive quadrant of the complex plane is shown. At $I = 8°$, the Floquet multipliers for $\lambda/D = 3.6$ exceed $|\mu| = 1$ at around $Re \simeq 350$. On further increasing the Reynolds number, the multipliers migrate towards, and then remain on the real axis as their imaginary component reduces to zero. For $Re \simeq 480$, a mode with a purely real multiplier is observed. As the angle of incidence is increased to $I = 16°$, a similar phenomenon is observed, with the multipliers coalescing on the real axis at $Re \simeq 290$.

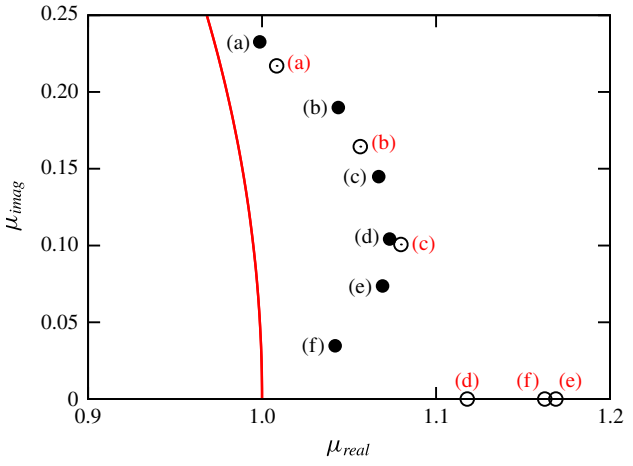

FIGURE 10. (Colour online) Locus of the Floquet multipliers on the complex plane for $\Gamma = 2.5$, $I = 16°$ for $Re = 285$ (●) and $Re = 290$ (○) at the specified values of spanwise wavelength. The unit circle ($|\mu| = 1$) is shown by the curved red line. For clarity, only the positive component of the complex-conjugate pair of the multipliers is shown in this figure. The values of λ/D are shown in black and red labels for $Re = 285$ and $Re = 290$, respectively for (a) $\lambda/D = 3.6$, (b) $\lambda/D = 3.9$, (c) $\lambda/D = 4.2$, (d) $\lambda/D = 4.5$, (e) $\lambda/D = 4.8$ and (f) $\lambda/D = 5.4$.

The spanwise perturbation contours of mode QPA are nearly, but not quite, identical after each period of shedding as the spanwise frequency (computed by $St_{3D} = \tan^{-1}(\mu_{imag}/\mu_{real})/(2\pi T_{2D})$, where T_{2D} is the period of BvK shedding obtained from the base flow computations) is of $O(10^{-3})$ (this can also be implicitly observed in figure 9(*a*,*b*), where the imaginary component of the multiplier has very low values). However, the perturbation contours are not identical several periods apart. Shown in figure 9(*c*,*d*) are the reconstructions of the streamwise perturbation vorticity at $\Gamma = 2.5$, $I = 8°$ and $Re = 400$, taken seventeen periods apart. The frequency (St_{3D}) of mode QPA at these parameter values is computed to be $\simeq 0.0063187$, which corresponds to a period of $\simeq 158.26$ non-dimensional time units or approximately thirty-four periods of shedding ($T_{2D} = 4.689$). After seventeen base flow periods, the mode has traversed half a wavelength in the spanwise direction.

At higher angles of incidence, the Reynolds number for onset of mode A (developed from mode QPA) varies with spanwise wavelength, and this makes it more difficult to accurately obtain the critical Reynolds number for onset of mode A by interpolation/extrapolation. Shown in figure 10 are the loci of the Floquet multipliers for $\Gamma = 2.5$, $I = 16°$ for $3.6 \leqslant \lambda/D \leqslant 5.4$. At $Re = 285$, mode QPA is unstable, as the multipliers have a non-zero imaginary component, with the maximum growth rate occurring at $\lambda/D = 4.5$. However, at $Re = 290$, the multipliers for $\lambda/D \gtrsim 4.5$ have a purely real Floquet multiplier.

As the angle of incidence is decreased from higher angles of incidence to zero, a similar behaviour is observed with the Floquet multipliers approaching the real axis. Shown in figure 11 are the loci of the Floquet multipliers in the complex plane. The values plotted here are normalised by the magnitude of the Floquet multiplier and hence lie on the unit circle (red curve). As the incident angle is decreased from $I = 12°$ to $I = 0°$, the multipliers gradually migrate towards the positive real axis.

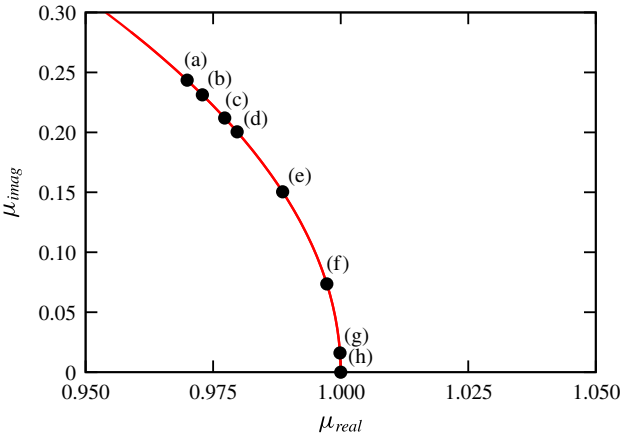

FIGURE 11. (Colour online) Locus of the normalised Floquet multipliers on the complex plane at the specified values for $\Gamma = 2.5$. The unit circle ($|\mu| = 1$) is shown by the curved red line. For clarity, only the positive component of the complex-conjugate pair of the multipliers is shown in this figure. The values chosen are close to the marginal stability curve for mode QPA: (a) $I = 12°$, $Re = 310$, $\lambda/D = 3.9$, (b) $I = 10°$, $Re = 330$, $\lambda/D = 3.6$, (c) $I = 9°$, $Re = 340$, $\lambda/D = 3.3$, (d) $I = 8°$, $Re = 360$, $\lambda/D = 3.3$, (e) $I = 6°$, $Re = 380$, $\lambda/D = 3.15$, (f) $I = 4°$, $Re = 400$, $\lambda/D = 3.0$, (g) $I = 2°$, $Re = 415$, $\lambda/D = 3.3$ and (h) $I = 0°$, $Re = 430$, $\lambda/D = 3.6$.

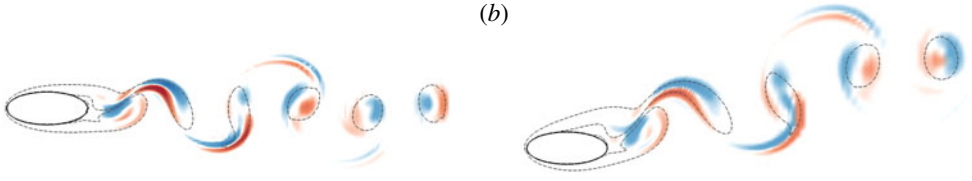

FIGURE 12. (Colour online) Visualisation of the spanwise perturbation vorticity contours in the wake of an elliptical cylinder of $\Gamma = 2.5$ for (*a*) $I = 0°$, $Re = 460$, $\lambda/D = 3.6$ and (*b*) $I = 16°$, $Re = 290$, $\lambda/D = 4.5$. Contour shading as per figure 6. Flow is from left to right in all images.

The wavelength of mode QPA at onset decreases from $\lambda_c/D \simeq 5.5$ at $I = 20°$ to $\lambda_c/D \simeq 3$ at $I = 4°$ (also see figure 8*f*). It may be recalled that mode $\widehat{\mathrm{B}}$ becomes unstable around $Re_c \simeq 330$, $\lambda_c/D \simeq 2$ at low angles of incidence and is unstable over a wide range of spanwise wavelengths ($1.6 \lesssim \lambda/D \lesssim 4$) at higher Reynolds numbers. This further makes it hard to discern the critical Reynolds number for mode QPA at lower angles of incidence and, thus, the predicted onset of this mode is shown by dashed lines in figure 7.

Shown in figure 12 are the spanwise perturbation contours of mode A at $I = 0°$ and the real mode at $I = 16°$ at a similar phase of the shedding cycle. From this figure, the real mode observed at Reynolds numbers beyond the decay of the imaginary component of the quasi-periodic mode at higher incident angles and mode A observed at zero angle of incidence by Leontini *et al.* (2015) are similar, and appear to be manifestations of the same instability. It is also likely that the two modes have the same physical mechanism leading to the growth of this instability.

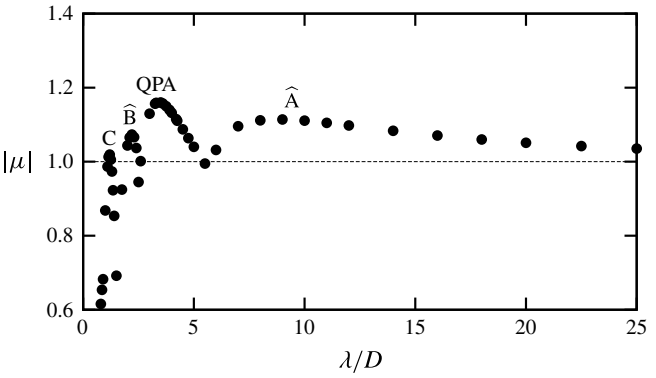

FIGURE 13. Variation of the Floquet multiplier with spanwise wavelength for the elliptical cylinder of $\Gamma = 2.5$, at $I = 8°$, $Re = 400$. The dashed line indicates neutral stability ($|\mu| = 1$). The three-dimensional modes which are unstable – modes C, $\widehat{\mathrm{B}}$, QPA and $\widehat{\mathrm{A}}$ are marked on this figure.

For a cylinder with a square cross-section, the pair of complex-conjugate Floquet multipliers observed at $I = 0°$ migrate and coalesce on the negative real axis as the angle of incidence is increased to 5.85° at a constant Reynolds number and spanwise wavelength. On further increasing the angle of incidence beyond this value, the pair of multipliers further split up as a stable and an unstable subharmonic mode (Blackburn & Sheard 2010; Sheard 2011). In contrast, for the elliptical cylinder case, a real mode is transformed to a quasi-periodic mode as the angle of incidence is increased (breaking of the Z_2 spatio-temporal symmetry), with a corresponding increase in the spanwise frequency of the three-dimensional mode.

To further validate the behaviour of mode QPA, a fully nonlinear three-dimensional direct numerical simulation was performed for $\Gamma = 2.5$, $I = 8°$, $Re = 400$. Sixty-four Fourier planes were employed to capture the flow over a spanwise distance of $z/D = 8$. This spanwise length was chosen to accommodate 1, 2, 4 and 7 wavelengths of modes $\widehat{\mathrm{A}}$, QPA, $\widehat{\mathrm{B}}$ and C, respectively. Figure 13 shows the variation of the Floquet multiplier with spanwise wavelength for this case. Mode QPA is the fastest-growing mode with highest valued Floquet multiplier occurring at $\lambda/D \simeq 3.5$. The two-dimensional base flow is used as a starting point with some low intensity white noise $O(10^{-4})$ added at the start of the simulation. Shown in figure 14(*a*,*b*) are the time histories of the streamwise (u) and spanwise (w) velocity components at a point $(x, y) = (1.58, 0.5)$, with the elliptical cylinder centred at the origin. The flow remains nearly two-dimensional for approximately one hundred time units, beyond which the growth of the spanwise velocity component is observed.

Figure 14(*c*–*f*) show the isosurfaces of streamwise vorticity in plan view at the specified time instants. At $\tau = 213$ (figure 14*c*), two wavelengths of $\lambda/D \simeq 4$ are observed across the span, which is in good agreement with the wavelength of mode QPA. At a later time of $\tau = 295$ (figure 14*c*), these structures have translated by half a wavelength in the spanwise direction compared to the earlier time instant. Furthermore, this spanwise shift is well predicted for a travelling wave with the period calculated from the stability analysis (also see figure 9). The streamwise vortices appear to shed obliquely (only marginally) in the near wake; however, further downstream they appear to be parallel to the incoming flow. These structures are consistent

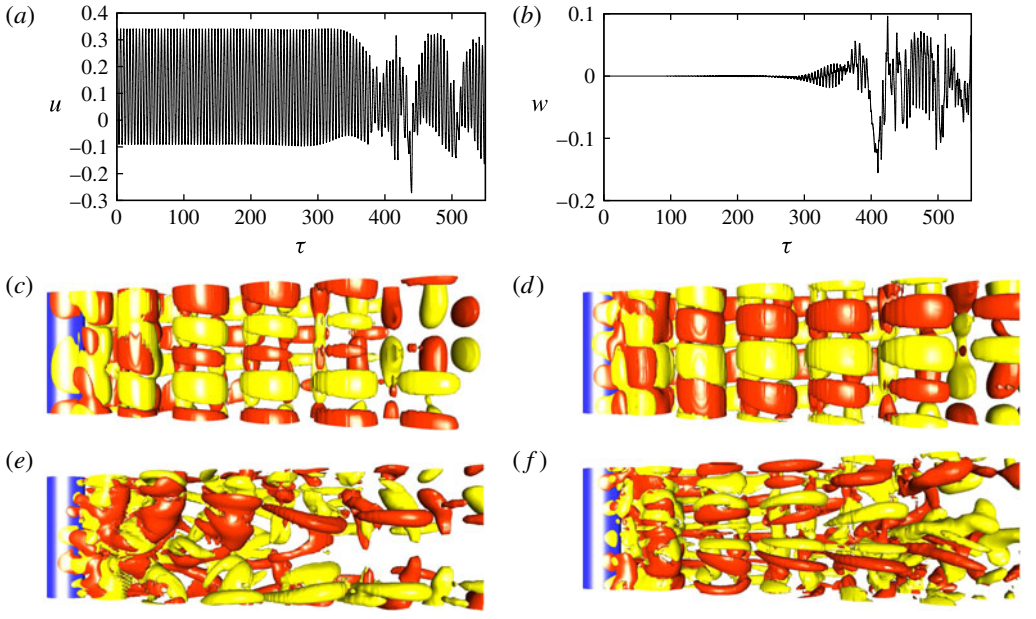

FIGURE 14. (Colour online) (*a*,*b*) Time histories of the streamwise and spanwise velocity components at a point in the wake ($(x, y) = (1.58, 0.5)$) of an elliptical cylinder of $\Gamma = 2.5$, $I = 8°$, $Re = 400$ for a cylinder of spanwise distance of $8D$. Visualisations of the streamwise vorticity (in red and yellow) in the wake of the cylinder (in blue) in plan view at (*c*) $\tau = 213$, (*d*) $\tau = 295$, (*e*) $\tau = 385$ and (*f*) $\tau = 426$. Flow is from left to right in images (*c*)–(*f*).

with figure 6(*b*) of Blackburn *et al.* (2005), where a travelling quasi-periodic wake is observed in the wake of a circular cylinder at $Re = 400$. As the flow saturates ($\tau \simeq 380$), the w velocity component begins to fluctuate with large magnitudes, resulting in irregular wake patterns, as seen in figure 14(*e*,*f*). At $\tau = 385$ (figure 14*e*), three-dimensional structures covering the entire span are observed in the near wake with dislocations in the subsequent vortex roller, leading to the breakup of the vortical structure (also see figure 34 of Williamson (1992)) further downstream. At a later time instant of $\tau = 426$ (figure 14*f*), smaller-scale structures bearing the hallmarks of mode B are observed in the near wake and disorderly vortex patterns occur in the far wake. (It may be recalled that the critical Reynolds number for the onset of mode B for these parameter values is $\simeq$472.) These observations are consistent with the three-dimensional computations of wakes behind inclined square cylinders (Sheard *et al.* 2009). Larger domain sizes and longer time histories would be required to quantify the disorderly wake structures; however, these would be computationally expensive to perform. Nonetheless, the fastest-growing mode predicted by the stability analysis, mode QPA, is observed in the saturating three-dimensional wake before chaotic flow ensues due to nonlinear interactions.

Also, the quasi-periodic mode observed in the wake of elliptical cylinders for $\Gamma \lesssim 1.8$ (mode QP) is different to that observed at higher aspect ratios (mode QPA). Mode QP which is observed at lower aspect ratios becomes unstable at Reynolds numbers beyond the onset of modes A and B and occurs at intermediate wavelengths of mode A and B. Mode QPA which occurs for $1.8 \lesssim \Gamma \lesssim 2.9$ becomes unstable

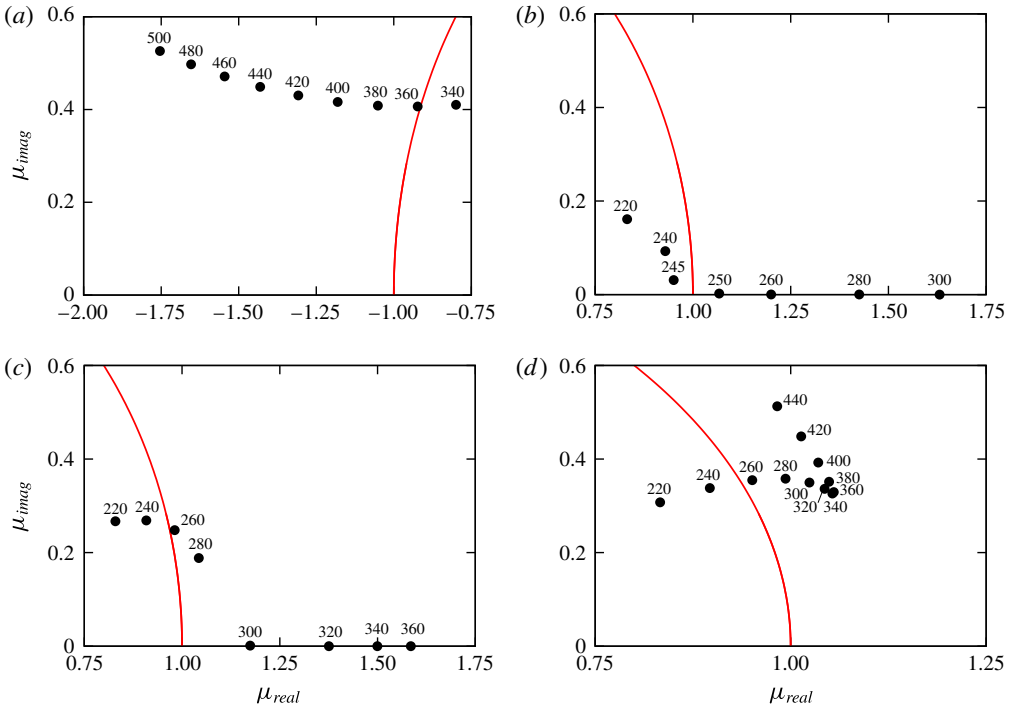

FIGURE 15. (Colour online) Locus of the Floquet multipliers on the complex plane for elliptical cylinders at an incident angle of $I = 16°$ for: (*a*) $\Gamma = 1.1$, $\lambda/D = 2$, (*b*) $\Gamma = 1.8$, $\lambda/D = 3.9$, (*c*) $\Gamma = 2.6$, $\lambda/D = 4.8$ and (*d*) $\Gamma = 3$, $\lambda/D = 4.8$ at the specified Reynolds numbers. The unit circle ($|\mu| = 1$) is shown by the curved red line. For clarity, only the positive component of the complex-conjugate pair of the multipliers is shown in this figure.

at Reynolds numbers prior to the onset of mode B, with a spanwise wavelength in the range of mode A instability. The real component of the Floquet multipliers of mode QP are negative, while that of mode QPA are positive. Shown in figure 15(*a*) are the loci of the Floquet multipliers for mode QP at $\Gamma = 1.1$, $I = 16°$, $\lambda/D = 2$. The imaginary component of the Floquet multiplier increases to higher values as the Reynolds number is increased beyond the transitional value. However, for $\Gamma \geqslant 1.8$, the quasi-periodic mode has a spanwise wavelength similar to that of mode A and the Floquet multipliers are real and positive as seen in figure 15(*b*).

Mode QPA was also observed for larger aspect ratios, for $\Gamma = 2.6$ and 2.8 for $I = 16°$, $\lambda/D = 4.8$, with the transformation to mode A occurring at $Re \simeq 300$ and 340, respectively. Figure 15(*c*,*d*) show the loci of the Floquet multipliers on the complex plane for $\lambda/D = 4.8$, $I = 16°$ for $\Gamma = 2.6$ and $\Gamma = 3$, respectively. For $\Gamma = 2.6$, mode QPA becomes unstable at $Re \simeq 255$ and the imaginary component of the Floquet multiplier decreases to zero as the Reynolds number is increased. However, for $\Gamma = 3$, $I = 16°$, such a transformation to mode A does not occur, with the imaginary component of the Floquet multiplier decreasing up to $Re = 360$ and then increasing rapidly to higher values with a further increases in Reynolds number, while the real component of the Floquet multiplier decreases gradually. The mode remains quasi-periodic at the maximum tested Reynolds number of $Re = 440$. A similar

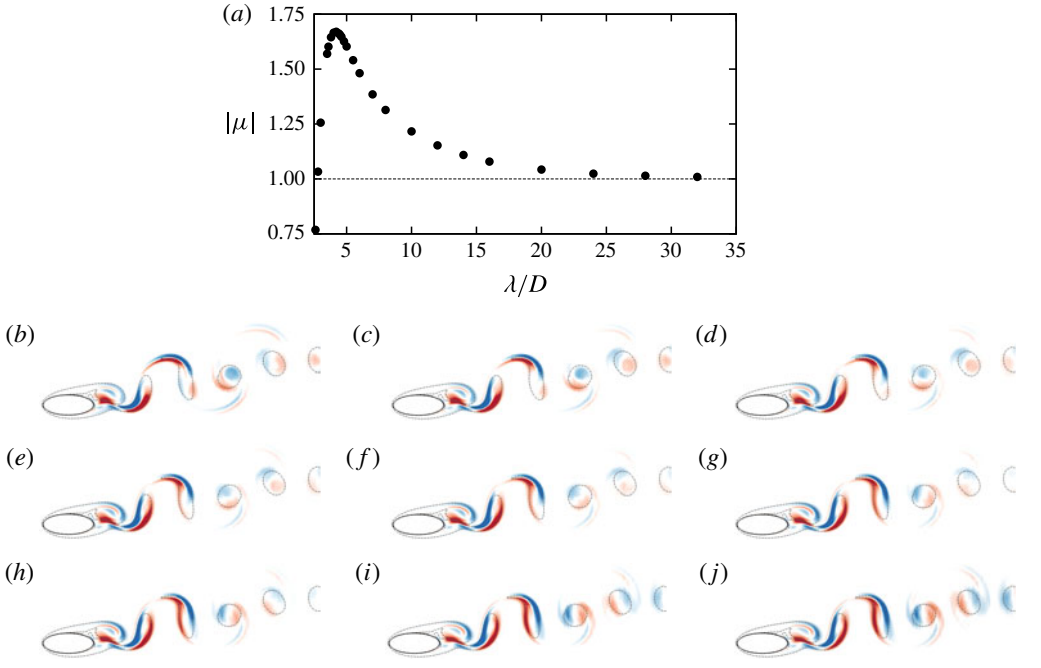

FIGURE 16. (Colour online) (*a*) Variation of the magnitude of the Floquet multiplier with spanwise wavelength at $\Gamma = 2.5$, $I = 12°$, $Re = 440$. The dashed line indicates neutral stability ($|\mu| = 1$). (*b–j*) Visualisation of the spanwise perturbation vorticity contours at the same instant in the vortex shedding cycle for spanwise wavelengths for (*b*) $\lambda/D = 4$, (*c*) $\lambda/D = 5$, (*d*) $\lambda/D = 6$, (*e*) $\lambda/D = 7$, (*f*) $\lambda/D = 8$, (*g*) $\lambda/D = 10$, (*h*) $\lambda/D = 12$, (*i*) $\lambda/D = 20$ and (*j*) $\lambda/D = 32$. Contour shading as per figure 6. Flow is from left to right in these images.

behaviour was observed at spanwise wavelengths of $\lambda/D = 3.6$ and 5.4 (not shown). Thus, mode QPA is unstable for $1.8 \lesssim \Gamma \lesssim 2.9$.

3.6. *Relationship between mode A and* $\widehat{\text{A}}$

Leontini *et al.* (2015) presented the relationship between modes A and $\widehat{\text{A}}$, indicating that both these modes are unstable for $\Gamma \gtrsim 1.2$ and share the same spatio-temporal characteristics. They further showed the variation of modes A and $\widehat{\text{A}}$ with increasing Reynolds numbers and pointed out that the two modes can be difficult to distinguish. Shown in figure 16 are the variation of the Floquet multiplier and the spanwise perturbation contours with spanwise wavelength for a case where $\Gamma = 2.5$, $I = 12°$, and $Re = 440$. For this case, the change from mode A to $\widehat{\text{A}}$ is gradual and a hard distinction cannot be made between the two modes. The structure of the perturbation in the third and fourth shed vortices appears to rotate between $\lambda/D = 4$ to $\lambda/D = 12$, covering 180° between these values. On further increasing the spanwise wavelength beyond $\lambda/D = 12$, the contours appear 'fixed' to this configuration. This gradual change is also observed in other bluff body wakes, where mode A is unstable over a large range of spanwise wavelengths; examples are the wake of square cylinders at zero angle of incidence (see figure 2 of Blackburn & Lopez (2003)), bluff bodies

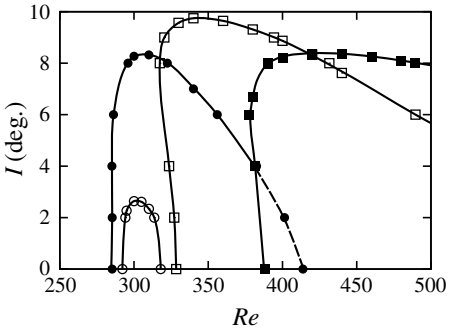

FIGURE 17. Unstable region of mode $\widehat{\mathrm{B}}$ in the $Re - I$ parameter space for $\Gamma = 1.8$ (○), $\Gamma = 2$ (●), $\Gamma = 2.5$ (□) and $\Gamma = 3$ (■). The onset of mode $\widehat{\mathrm{B}}$ is delayed to higher Reynolds numbers as the aspect ratio is increased beyond $\Gamma = 2$. The dashed line of mode $\widehat{\mathrm{B}}$ for $\Gamma = 2$ at low incident angles indicates the values have been extrapolated using the quadratic fit method employed in Leontini *et al.* (2015).

with elliptical leading edges (see figure 7*a* of Ryan *et al.* (2005)) and inclined flat plates ($\Gamma = 0$) at $I = 20°$ (see figure 2 of Yang *et al.* (2013)).

3.7. *Unstable region of mode* $\widehat{\mathrm{B}}$

Mode $\widehat{\mathrm{B}}$ first becomes unstable for $\Gamma \gtrsim 1.75$ for $Re \simeq 285$, $I = 0°$ (Leontini *et al.* 2015). The range of Reynolds number over which mode $\widehat{\mathrm{B}}$ is unstable increases with aspect ratio and for $\Gamma \gtrsim 1.9$, mode $\widehat{\mathrm{B}}$ is the first three-dimensional mode to become unstable as Reynolds number is increased. A similar observation was made by Ryan *et al.* (2005), Thompson *et al.* (2006*b*), where this mode precedes the onset of mode A in the wake of bluff bodies with elliptical leading edges of $\Gamma = 5$. Figure 17 shows the unstable region of mode $\widehat{\mathrm{B}}$ for $\Gamma \leqslant 3$. The upper limit of mode $\widehat{\mathrm{B}}$ at lower angles of incidence was obtained using the method employed by Leontini *et al.* (2015), as the growth rates of mode QPA were significantly higher and the multiplier of a waning mode $\widehat{\mathrm{B}}$ could not be accurately resolved. At $\Gamma = 1.8$, mode $\widehat{\mathrm{B}}$ exists for $I \lesssim 3°$, $290 \leqslant Re \leqslant 315$, and for a marginal increase in the aspect ratio to $\Gamma = 2$, the range of Reynolds number and incident angles over which this mode is unstable increases to $285 \leqslant Re \lesssim 415$ and $I \lesssim 9°$, respectively. As the aspect ratio is further increased to $\Gamma = 2.5$, the onset of mode $\widehat{\mathrm{B}}$ is delayed to higher Reynolds numbers and is unstable for $I \lesssim 10°$. At a larger aspect ratio of $\Gamma = 3$, mode $\widehat{\mathrm{B}}$ is found to be unstable for $I \lesssim 9°$, but over a much larger range of Reynolds number. (Note that the $\Gamma = 3$ case was investigated for mode $\widehat{\mathrm{B}}$ for $I \leqslant 10°$ with adequate spatial resolution.) While the critical spanwise wavelength at onset of this mode was found to decrease with aspect ratio (Leontini *et al.* 2015), a marginal increase was observed with an increase in the angle of incidence for a given aspect ratio (also see figure 8*c*).

Mode $\widehat{\mathrm{B}}$ is observed to be unstable over a range of spanwise wavelengths as Reynolds number is increased beyond the critical value at a given incident angle. Figure 18(*a*) shows the contour plot of the Floquet multiplier for $1.6 \leqslant \lambda/D \leqslant 2.6$ at $\Gamma = 2.5$ when the incident angle is held constant at $I = 8°$ and Reynolds number is gradually increased. At this incident angle, the maximum value of the Floquet multiplier of this mode is observed at $Re \simeq 380$ for a spanwise wavelength $\lambda/D \simeq 2.2$.

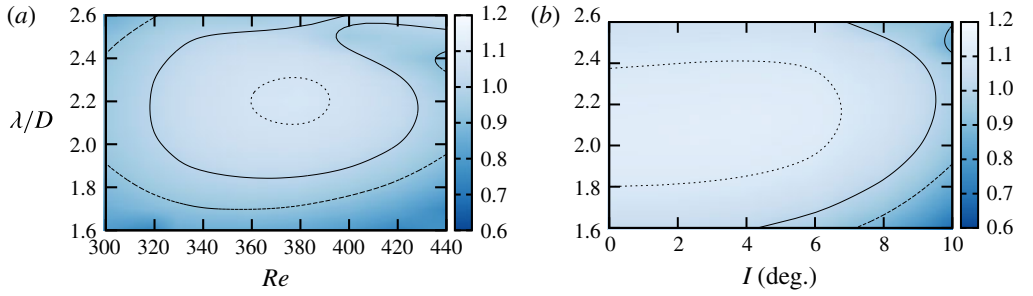

FIGURE 18. (Colour online) Contour plots of the Floquet multiplier of mode $\widehat{\mathrm{B}}$ for $\Gamma = 2.5$: (*a*) as a $f(Re, \lambda/D)$ at a constant incident angle of $I = 8°$ and (*b*) as a $f(I, \lambda/D)$ at a constant Reynolds number of $Re = 360$. Contour lines in (*a*) are at $|\mu| = 1.075$ (thin dashed lines), 1 (continuous line) and 0.925 (thick dashed lines). Contour lines in (*b*) are at $\mu = 1.15$ (thin dashed lines), 1 (continuous line) and 0.9 (thick dashed lines).

The Floquet multiplier decreases to lower values at as the Reynolds number is increased. At higher Reynolds numbers, we observe mode QPA becoming unstable at wavelengths of $\lambda/D = 2.6$ (top right of the figure). In figure 18(*b*), the Reynolds number is held constant and the incident angle is increased from $0° \leqslant I \leqslant 0°$, the maximum Floquet multiplier of this mode occurs at $I \simeq 4°$. The Floquet multiplier decreases with a further increase in incident angle. This behaviour is consistent with the closed regions formed by mode $\widehat{\mathrm{B}}$ in the $Re - I$ parameter space.

3.8. *Behaviour of mode C and mode QP*

For elliptical cylinders $\Gamma \lesssim 2$, mode C occurs at higher values of incident angles when the wake is no longer symmetrical. This behaviour is very similar to that observed for an inclined flat plate or a triangular cylinder, where mode C is observed at increasing lower Reynolds numbers as the incident angle is increased (Yang *et al.* 2013; Ng *et al.* 2016), and also to that of a subharmonic mode becoming unstable in the wake of a rotating cylinder as the rotation rate is increased (Rao *et al.* 2013*a*, 2015*a*). Essentially, the Z_2 spatio-temporal symmetry needs to be broken for subharmonic modes to occur (Blackburn & Sheard 2010). For the elliptical cylinder of $\Gamma \lesssim 2$, mode C is observed to become unstable in the same range of spanwise wavelengths as that of the unstable QP mode; usually at the lower range spanwise wavelengths of mode QP. The critical Reynolds number for mode QP is lower than that of mode C for $I \leqslant 20°$. Shown in figure 19(*a*) is the contour plot of the Floquet multiplier with spanwise wavelength with Reynolds number for $\Gamma = 1.5, I = 16°$. Mode QP becomes unstable at $Re_c \simeq 335$, $\lambda_c/D \simeq 2.1$ and mode C at $Re_c \simeq 381$, $\lambda_c/D \simeq 1.85$. The growth rate of mode C exceeds that of mode QP for small increments in Reynolds numbers. A similar phenomenon was observed in the wake of inclined square cylinders (Sheard *et al.* 2009; Sheard 2011) and in the wake of rings (Sheard, Thompson & Hourigan 2005*a*; Sheard *et al.* 2005*b*) and has been documented previously in Blackburn & Sheard (2010). For the inclined square cylinder, they show the transformation of from mode QP to mode C at a constant Reynolds number and spanwise wavelength as the incident angle is increased from $I = 0°$ to $I = 8°$; with mode QP multiplier first becoming stable to perturbations as the incident angle is increased from $I = 0°$ and coalescing on the real axis as stable subharmonic modes at $I = 5.85°$, and finally

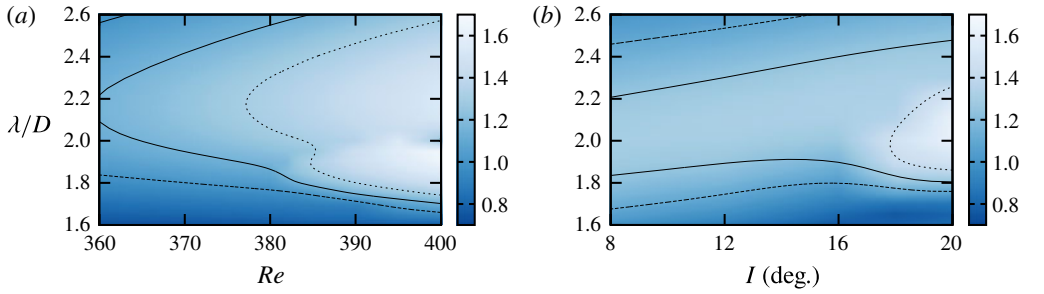

FIGURE 19. (Colour online) Contour plots of the Floquet multipliers for mode QP and mode C for $\Gamma = 1.5$: (*a*) as a $f(Re, \lambda/D)$ at a constant incident angle at $I = 16°$ and (*b*) as a $f(I, \lambda/D)$ at a constant Reynolds number of $Re = 380$. Contour lines in (*a*) are at $|\mu| = 1.3$ (thin dashed lines), 1.15 (continuous line) and 1 (thick dashed lines) and in (*b*) are at $|\mu| = 1.4$ (thin dashed lines), 1.25 (continuous line) and 1.1 (thick dashed lines).

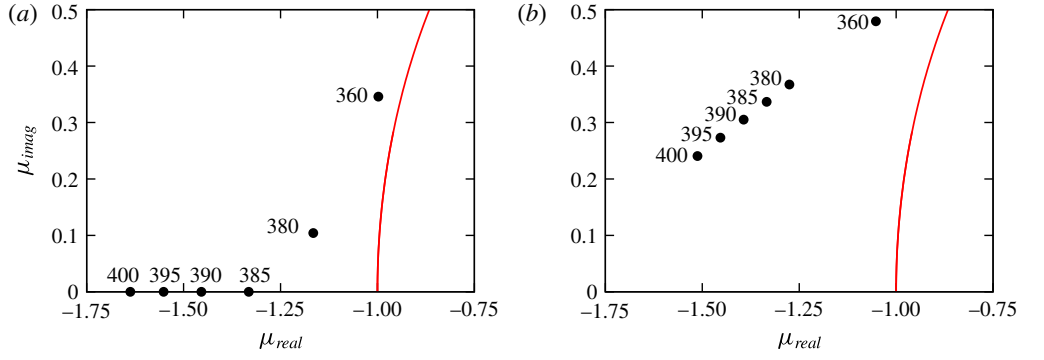

FIGURE 20. (Colour online) Locus of the Floquet multipliers on the complex plane for $\Gamma = 1.5, I = 16°$ at the specified Reynolds numbers for spanwise wavelengths of (*a*) $\lambda/D = 1.9$ and (*b*) $\lambda/D = 2.15$. The unit circle ($|\mu| = 1$) is shown by the curved red line. For clarity, only the positive component of the complex-conjugate pair of the multipliers is shown in this figure.

becoming unstable at $I = 7.5°$. Shown in figure 19(*b*) is the contour plot of the Floquet multipliers at $\Gamma = 1.5$ with incident angle, at a constant Reynolds number of $Re = 380$. The maximum growth rate of mode QP occurs at increasing values of spanwise wavelength as the incident angle is increased from $I = 8°$. Mode C becomes unstable for $I \gtrsim 16°$ at lower values of spanwise wavelength and has a higher growth rate as compared with mode QP. This is again similar to the behaviour observed in the wake of square cylinders at low incident angles (Sheard 2011).

Shown in figure 20(*a*,*b*) are the loci of the Floquet multipliers at the specified Reynolds number on the complex plane for $\Gamma = 1.5$, $I = 16°$ for $\lambda/D = 1.9$ and $\lambda/D = 2.15$, respectively. For $\lambda/D = 1.9$, the transformation of mode QP to mode C occurs as Reynolds number is increased; and for $\lambda/D = 2.15$, the quasi-periodic mode does not undergo the transformation to a subharmonic mode for the Reynolds numbers considered here. Nonetheless, these a plots show the dependence of both Reynolds number and spanwise wavelength for such transformations to occur.

Shown in figure 21(*a*,*b*) is the variation of spanwise wavelength at which the maximum Floquet multipliers of modes QP and mode C occur at $I = 18°$ for $\Gamma = 1.5$

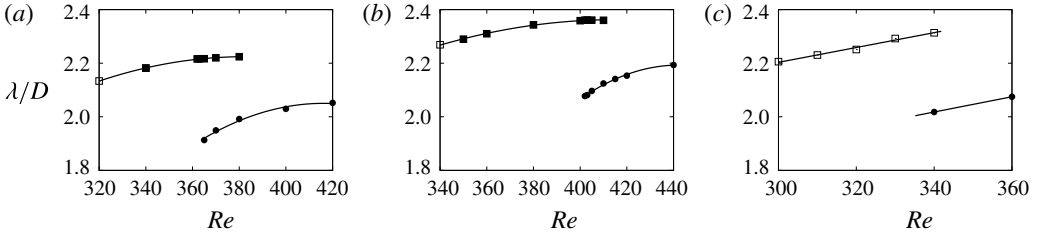

FIGURE 21. Variation of the dominant spanwise wavelength of mode C (●) and mode QP (□, ■) at $I = 18°$ for (*a*) $\Gamma = 1.5$, (*b*) $\Gamma = 2$ and (*c*) $\Gamma = 1.5, I = 22°$. Open symbols indicate values when the mode is stable to perturbations ($\mu < 1$), while filled symbols indicate values where Floquet multipliers are unstable ($\mu \geqslant 1$). Lines are best fits to the measured values.

and $\Gamma = 2$, respectively. For $\Gamma = 1.5$ ($\Gamma = 2$), mode QP becomes unstable for $Re \gtrsim 332$ ($Re \gtrsim 344$) and mode C is observed for $Re \gtrsim 365$ ($Re \gtrsim 402$). The dominant wavelength for both modes increases marginally with Reynolds number. For $\Gamma = 1.5$ ($\Gamma = 2$), both mode C and mode QP have distinct peaks in the $\mu - \lambda/D$ space for $365 \leqslant Re \leqslant 380$ ($402 \leqslant Re \leqslant 410$), and beyond $Re = 380$ ($Re = 415$), a clear peak for mode QP is not observed. For $\Gamma = 1.5$, $I \leqslant 20°$, mode C becomes unstable to perturbations at Reynolds numbers beyond the onset of mode QP. However, at a slightly larger incident angle of $I = 22°$, mode C becomes unstable prior to mode QP as indicated in figure 21(*c*). For $Re \gtrsim 340$, mode C becomes unstable, while the mode QP branch is still stable to perturbations. Beyond $Re \gtrsim 340$, no discernible peak is observed for mode QP, although the QP branch was found to be unstable for $Re \gtrsim 360$. This is not surprising as the Floquet multiplier of mode C is much higher than compared with that of mode QP. This cross over is also apparent from the parameter space plot (see figure 4), where the Re_c of mode C decreases with increasing incident angle, while that of mode QP increases to higher values of Reynolds numbers.

For $\Gamma = 2.5$, mode C is unstable over an enclosed region in the $Re - I$ parameter space. Shown in figure 22(*a*,*b*) are the contour plots of the Floquet multiplier over spanwise wavelength at a constant incident angle of $I = 8°$ and a constant Reynolds number of $Re = 400$, respectively. In these plots, the Floquet multiplier of mode C increases as Reynolds number and incident angle is shown to initially increase, before decreasing with further increases in Reynolds numbers and/or incident angle. Figure 22(*a*) shows that the spanwise wavelength at which the maximum Floquet multiplier of mode C occurs does not depend strongly on the Reynolds number at the incident angle considered, while figure 22(*b*) shows that the maximum Floquet multiplier of mode C occurs at $I \simeq 9°$ at $Re = 400$. Similar closed regions of instability of mode C in the $Re - \lambda/D$ plots have been observed in the wakes of flat plates at incident angles of 20° and 25° (Yang *et al.* 2013). For the flat plate inclined at 20° to the flow, mode C is unstable for $400 \leqslant Re \leqslant 510$, and for the flat plate inclined at 25°, the onset of mode C occurs at a lower Reynolds number of $Re \simeq 266$ and is unstable for $Re \lesssim 305$. As a result of the flow becoming aperiodic for $Re \gtrsim 305$, they double the sampling period for their stability analysis and observe that the unstable mode now has positive real multipliers, which they call mode D. Mode D is observed for $305 \leqslant Re \leqslant 330$, and together with the subharmonic mode, mode C, observed for $Re \leqslant 305$, form a closed region in the $Re - \lambda/D$ plot. Mode C and mode D have

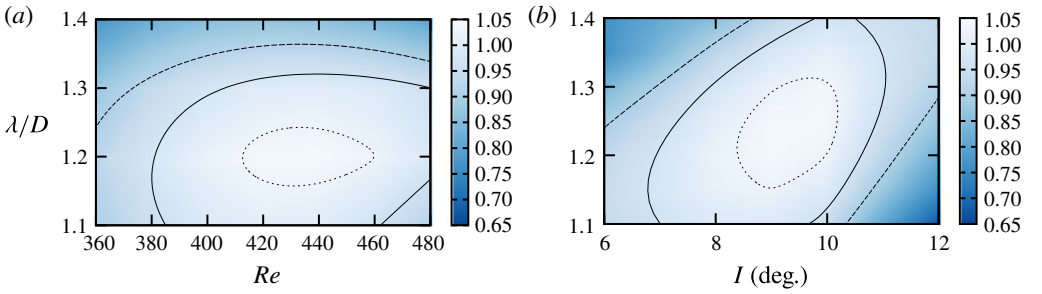

FIGURE 22. (Colour online) Contour plots of the Floquet multiplier of mode C for $\Gamma = 2.5$: (*a*) as a $f(Re, \lambda/D)$ at a constant incident angle of $I = 8°$ and (*b*) as a $f(I, \lambda/D)$ at a constant Reynolds number of $Re = 400$. Contour lines in (*a b*) are at $|\mu| = 1.02$ (thin dashed lines), 0.96 (continuous line) and 0.9 (thick dashed lines).

identical perturbation contours in the near wake as seen in figure 7(*c–e*) of their study. Furthermore, the spanwise wavelength at which the maximum growth occurs does not change across the two modes ($\lambda/D \simeq 0.8$).

3.9. *Mode E instability*

Using a steady solver, the onset of the three-dimensional modes is investigated by perturbing the stabilised based flows, i.e. steady base flows that would naturally be periodic without stabilisation. Previously, such studies were used to identify the three-dimensional mode that occurred when the BvK vortex shedding was suppressed (Rao *et al.* 2015*a*, 2016). This three-dimensional mode, named mode E, in the alphabetical order of the modes discovered in the wake of rotating cylinders (Rao *et al.* 2013*a*,*b*, 2015*a*), and experimentally observed in Radi *et al.* (2013), occurs in the wake of elliptical cylinders as the aspect ratio is increased and also when the angle of incidence is changed. It may be recalled that mode E has a positive real multiplier and the structure of the mode bears close resemblance to the modes observed in bluff body flows near walls (Stewart *et al.* 2010; Rao *et al.* 2011, 2013*c*), where the onset of three-dimensionality occurs prior to the onset of unsteady flow.

Shown in figure 23(*a*) is the variation of the critical Reynolds number and spanwise wavelength of the mode E instability with increasing aspect ratio. As the aspect ratio is increased from $\Gamma = 1$ to $\Gamma = 4$, the onset of the critical Reynolds number for mode E increases from $Re_c \simeq 95$ to $Re_c \simeq 262$, while the critical wavelength decreases from $\lambda_c/D \simeq 6$ at $\Gamma = 1$ to $\lambda_c/D \simeq 4$ at $\Gamma = 4$. Shown in figure 23(*b*) are the variations of the critical Reynolds number and wavelength with increasing incident angle for the aspect ratios investigated of $\Gamma = 1.1$, 1.5, 2 and 2.5. For small values of aspect ratio, the variation in critical Reynolds number with incident angle is small, and on increasing the aspect ratio to $\Gamma = 2.5$, the critical Reynolds number decreases from $Re_c \simeq 165$ at $I = 0°$ to $Re_c \simeq 97$ at $I = 20°$. The corresponding variation in the critical spanwise wavelength at low aspect ratios is small while for higher aspect ratios, the variation is more pronounced, as shown in figure 23(*c*). The critical spanwise wavelength increases marginally for $\Gamma = 1.1$ with angle of incidence, while for $\Gamma = 2.5$, it varies from $\lambda_c/D \simeq 4.7$ at $I = 0°$ to $\lambda_c/D \simeq 7$ at $I = 20°$.

Shown in figure 24(*a*,*b*) are the spanwise perturbation contours of mode E instability in the wake of elliptical cylinders at the specified parametric values. As the aspect ratio increases, the width of the wake reduces and the shear layers appear elongated

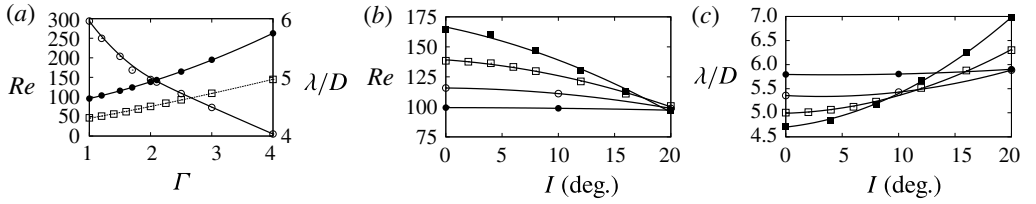

FIGURE 23. (*a*) Marginal stability diagrams of the mode E instability showing the variation of the critical Reynolds number (●), spanwise wavelength (○) and the critical Reynolds number for the onset of unsteady flow (□) with varying aspect ratios at $I = 0°$. (*b*) The variation of the critical Reynolds number with angle of incidence is shown for $\Gamma = 1.1$ (●), $\Gamma = 1.5$ (○), $\Gamma = 2$ (□) and $\Gamma = 2.5$ (■). The critical Reynolds number for the onset of this mode decreases to lower values as the angle of incidence is increased. (*c*) Variation of the critical spanwise wavelength of the mode E instability at onset with angle of incidence for the aspect ratios in (*b*). Lines are best fits to the measured values. Plots reproduced from figures 3 and 4 of Rao *et al.* (2016).

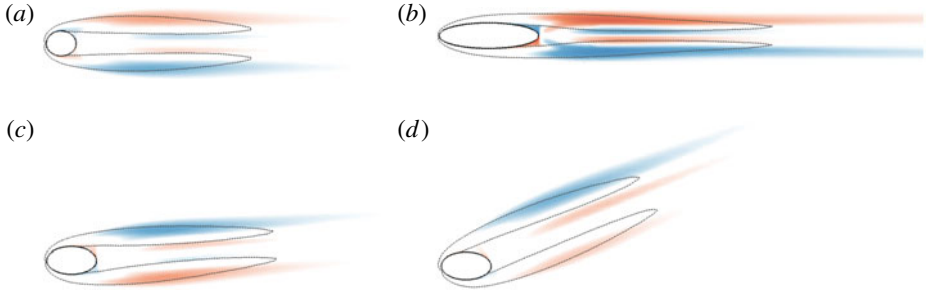

FIGURE 24. (Colour online) Visualisation of the spanwise perturbation vorticity contours for the mode E instability in the wake of an elliptical cylinder for (*a*) $\Gamma = 1.2, I = 0°, Re = 110, \lambda/D = 6$, (*b*) $\Gamma = 4, I = 0°, Re = 280, \lambda/D = 4$, (*c*) $\Gamma = 2, I = 4°, Re = 140, \lambda/D = 5$ and (*d*) $\Gamma = 2, I = 20°, Re = 110, \lambda/D = 6.5$. Contour shading as per figure 6. Flow is from left to right in these images. Images reproduced from figures 3 and 4 of Rao *et al.* (2016).

for the zero angle of incidence cases. Figure 24(*c*,*d*) show the perturbation contours as the angle of incidence is increased for $\Gamma = 2$. In both these cases, the structure of the perturbation is similar, although the underlying base flows have changed. For more details on the mode E instability, the reader is referred to Rao *et al.* (2016), where a wide range of bluff body geometries has been investigated and their instability mechanisms discussed.

3.10. *Three-dimensional simulations*

A few three-dimensional simulations were performed to investigate the nonlinear behaviour of the three-dimensional modes and to compare with the results of the linear stability analysis. Domain sizes of $z/D = 16$ with 128 Fourier planes in the spanwise direction were used in the three-dimensional simulations described henceforth. Shown in figure 25(*a*,*b*) are the velocity traces at a point in the flow for $\Gamma = 1.6, I = 0°, Re = 300$ in the streamwise and spanwise direction, respectively, while figure 25(*c*–*e*) show the streamwise vorticity contours in plan view. At these

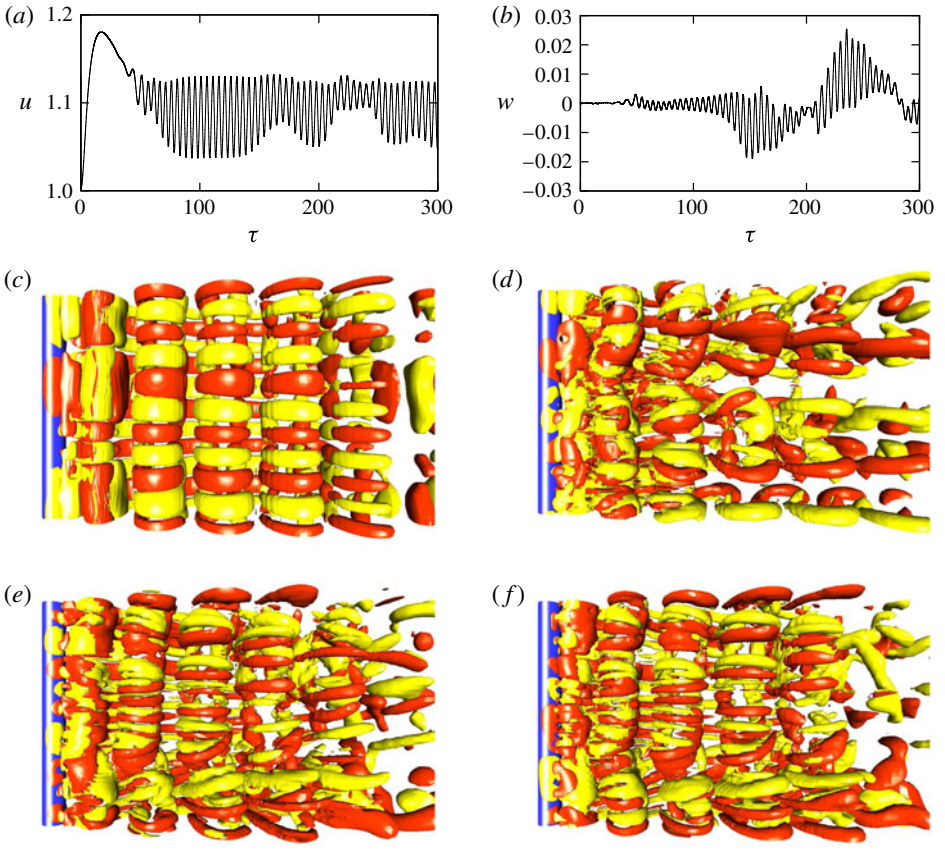

FIGURE 25. (Colour online) (*a*,*b*) Time histories of the streamwise and spanwise velocity components at a point in the wake ($(x, y) = (1.76, 1.76)$) of an elliptical cylinder of $\Gamma = 1.6$, $I = 0°$, $Re = 300$ for a cylinder of spanwise distance of $16D$. Visualisations of the streamwise vorticity (in red and yellow) in the wake of the elliptic cylinder (in blue) in plan view at (*c*) $\tau = 103$, (*d*) $\tau = 172$, (*e*) $\tau = 257$ and (*f*) $\tau = 261$. Flow is from left to right in images (*c–f*).

parameter values, linear stability analysis predicts the critical Reynolds number for the transition to three-dimensionality of mode $\widehat{\text{A}}$, A and B at $Re_c \simeq 251$, 264 and 335, respectively (Leontini *et al.* 2015). In the saturating phase at $\tau = 103$ (figure 25*c*), we observe mode $\widehat{\text{A}}$ type structure in the first wake vortex, and five wavelengths of mode A in the subsequent downstream vortex rollers. Once the wake has saturated (figure 25*d*), the wake is no longer orderly due to vortex dislocations, although mode A-type structures are clearly discernible in the third and fourth rollers (also see Williamson (1989, 1992, 1996*b*), Ling & Zhao (2009), Behara & Mittal (2010), Jiang *et al.* (2016*a*,*b*) and others). At a much later time at $\tau = 257$ (figure 25*e*), streamwise vortices similar reminiscent of mode B are found to dominate much of the wake, with little or no remnants of mode $\widehat{\text{A}}$ or mode A structures. This premature occurrence of mode B-type structures is not uncommon as previous numerical (Akbar, Bouchet & Dušek 2014), and experimental results (Williamson 1996*a*) for a circular cylinder show mode B occurring at $Re \simeq 220$ although linear stability analysis predicts the onset of mode B to occur at much higher Reynolds number of $Re \simeq 260$ (Barkley &

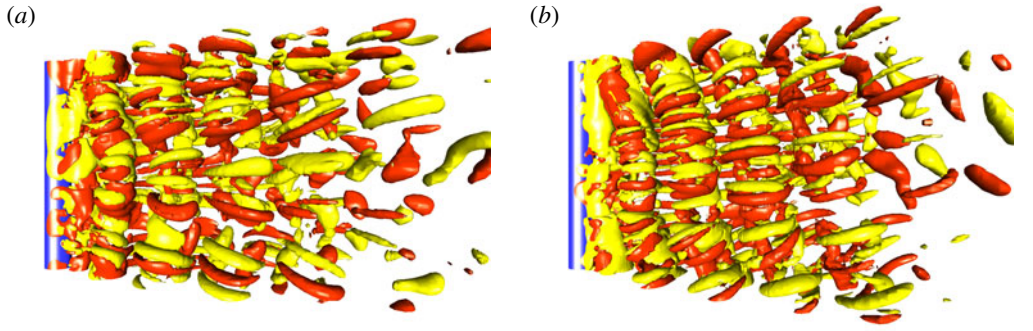

FIGURE 26. (Colour online) Visualisations of the streamwise vorticity (in red and yellow) in the wake of the elliptic cylinder (in blue) in plan view at $\Gamma = 2, I = 12°, Re = 320$ for a cylinder of spanwise distance of $16D$, at (*a*) $\tau = 276$ and (*b*) $\tau = 1903$. Flow is from left to right in these images.

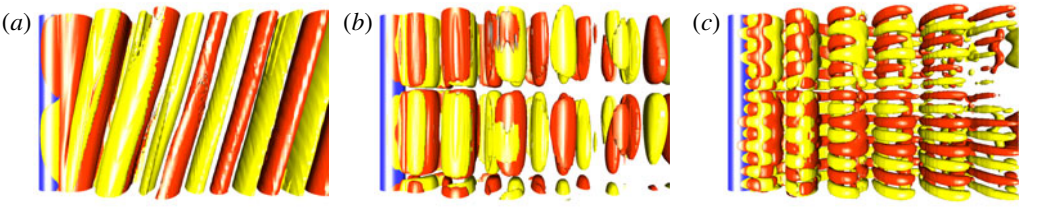

FIGURE 27. (Colour online) Visualisations of the streamwise vorticity (in red and yellow) in the wake of the elliptic cylinder (in blue) in plan view at $\Gamma = 2.25, I = 0°$ for a cylinder of spanwise distance of $16D$, at (*a*) $Re = 300, \tau = 618$, (*b*) $Re = 320, \tau = 649$ and (*c*) $Re = 320, \tau = 1079$. Flow is from left to right in these images.

Henderson 1996). On careful observation of figure 25(*e*), there appears to be a site of dislocation at the bottom left of the image, leading to the second vortex roller being shed slightly obliquely to the flow (also see Williamson (1989)). However, this oblique shedding is not sustained as the vortices are shed parallel to the flow approximately one period later at $\tau = 261$ (figure 25*f*).

Figure 26 shows the plan view of the wake at two time periods at $\Gamma = 2$, $I = 12°$, $Re = 320$, an increase in the aspect ratio, incident angle and Reynolds number as compared to the previous example. At $\tau = 276$, mode $\widehat{\mathrm{A}}$ can be observed growing on the first vortex, while a smaller wavelength mode can be observed to grow on the vortices downstream. However, at a much later time, $\tau = 1903$, oblique vortex shedding is observed; with much smaller-scale structures, with wavelengths similar to mode B appear in the near wake on these obliquely shed vortices. However, no discernible mode structures can be observed downstream due to the chaotic nature of the wake.

Oblique shedding with pure mode $\widehat{\mathrm{A}}$ instability has also been observed in the saturated wake for $\Gamma = 2.25$, $I = 0°$, $Re = 300$ (figure 27*a*). For this case, linear stability analysis predicts the flow to be two-dimensional, with the onset of mode $\widehat{\mathrm{B}}$ and mode $\widehat{\mathrm{A}}$ predicted at $Re_c \simeq 303$ and $Re \gtrsim 320$, respectively. One wavelength of the mode $\widehat{\mathrm{A}}$ instability is observed spanning the width of the cylinder in the near

wake and the vortex rollers are inclined to the flow. It may be recalled that Leontini *et al.* (2015) presented similar three-dimensional simulations at $\Gamma = 2$, $Re = 350$ showing mode $\widehat{\mathrm{A}}$ in the wake although linear stability analysis predicted mode $\widehat{\mathrm{B}}$ to be the most unstable mode. At a slightly higher Reynolds number of $Re = 320$ (figure 27*b*), parallel shedding is observed in the wake with one wavelength of mode $\widehat{\mathrm{A}}$ instability covering the entire span (note that these structures are very similar to the three-dimensional reconstructions of mode G in figure 22*g* of Rao *et al.* (2013*a*)); while at a much later time $\tau = 1079$ (figure 27*c*), mode $\widehat{\mathrm{B}}$-type structures can be observed in the wake. It may be recalled that parallel and oblique vortex shedding has previously been observed numerically in the fully developed wake of rotating and non-rotating circular cylinders (Mittal & Sidharth 2014; Navrose, Meena & Mittal 2015), and in the wake of inclined flat plates (Yang *et al.* 2012) for incident angles $I \gtrsim 20°$.

4. Conclusion

The three-dimensional stability for the flow past an elliptical cylinder for $\Gamma \leqslant 4$, $Re \leqslant 500$ was investigated for incident angles $I \leqslant 20°$. For low-aspect-ratio elliptical cylinders, the three-dimensional transition scenario closely resembles that of a circular cylinder with the onset of mode A, followed by mode B, and finally a quasi-periodic mode, mode QP, on increasing the Reynolds number. The order of the transition is not altered by the increase in angle of incidence, although the critical values are marginally lower for the synchronous modes, modes A and B; the critical value of mode QP marginally increases with increase in angle of incidence.

As the aspect ratio of the cylinder is increased to $\Gamma = 1.5$, the onset of a long-wavelength three-dimensional mode, mode $\widehat{\mathrm{A}}$, is observed. The critical Reynolds number for the onset of mode $\widehat{\mathrm{A}}$ occurs close to the onset of mode A and they share the same spatio-temporal characteristics. The onset of modes $\widehat{\mathrm{A}}$, A and B occurs at Reynolds numbers lower than for the circular cylinder case, while that of mode QP increases to higher Reynolds numbers as the angle of incidence is increased. For $I \gtrsim 12°$, a subharmonic mode is observed due to the increasing asymmetry in the flow. The onset of mode C occurs at lower Reynolds numbers as the angle of incidence is increased.

The transition scenario for $\Gamma = 2$ is similar to the $\Gamma = 1.5$ case, but with the unstable region of mode $\widehat{\mathrm{B}}$, which forms a closed region in the $Re - I$ parameter space. As the aspect ratio is increased, the unstable region of mode $\widehat{\mathrm{B}}$ expands, with the mode being unstable over a large range of Reynolds numbers. However, mode $\widehat{\mathrm{B}}$ is not observed beyond $I \geqslant 10°$ at larger aspect ratios. The onset of mode C is delayed to higher incident angles compared with the $\Gamma = 1.5$, with mode C being observed beyond $I \simeq 18°$.

For $1.8 \lesssim \Gamma \lesssim 2.9$, a new three-dimensional mode, mode QPA, is observed. As the flow symmetry is broken, mode A transforms to a quasi-periodic mode, with the imaginary component of the Floquet multiplier increasing with the increase in the angle of incidence. In addition, for a given angle of incidence, the imaginary component of the quasi-periodic mode decreases to zero as the Reynolds number is increased, giving way to a real mode. This real mode has a perturbation structure and spatio-temporal symmetries similar to mode A. The frequency of the quasi-periodic mode computed from the stability analysis is in good agreement with that predicted from a three-dimensional simulation.

Mode	λ/D	Nature of μ	Base flow	Symmetry
A	[4–4.5]	Real and positive	BvK shedding	$u(x, y, z, t) = u(x, y, z + n\lambda, t + T)$
$\widehat{\text{A}}$	[6–50]	Real and positive	BvK shedding	$u(x, y, z, t) = u(x, y, z + n\lambda, t + T)$
B	[0.8–1.05]	Real and positive	BvK shedding	$u(x, y, z, t) = u(x, y, z + n\lambda, t + T)$
$\widehat{\text{B}}$	[2–2.5]	Real and positive	BvK shedding	$u(x, y, z, t) = u(x, y, z + n\lambda, t + T)$
C	[1.1–2.1]	Real and negative	BvK shedding	$u(x, y, z, t) = u(x, y, z + n\lambda, t + 2T)$
E	[5.5–7]	Linear growth	Steady	$u(x, y, z, t) = u(x, y, z + n\lambda)$
QP	[1.8–2.4]	Complex	BvK shedding	$u(x, y, z, t) = u(x, y, z + n\lambda, t + T_{3D})$
QPA	[3–5.5]	Complex	BvK shedding	$u(x, y, z, t) = u(x, y, z + n\lambda, t + T_{3D})$

TABLE 1. Summary of the three-dimensional modes showing the characteristic wavelength at onset, nature of the Floquet multiplier (μ), the periodicity of the two-dimensional base flow and the spatial symmetries of these modes with respect to the streamwise velocity, u.

For $\Gamma = 2.5$, mode C forms a closed region in the parameter space. The critical Reynolds number for the transitions of the three-dimensional modes is delayed to higher Reynolds numbers at low angles of incidence due to the streamlining of the cylinder, while the critical values at higher incident angles decrease rapidly as the angle of incidence is increased, due to the increased bluffness of the cylinder.

While these three-dimensional bifurcation scenarios are presented for the unsteady flow, the artificially stabilised base flows were also tested for their three-dimensional stability. A three-dimensional steady mode, mode E, was observed on these base flows at Reynolds numbers where the flow would be naturally unsteady. The variations of critical Reynolds number and spanwise wavelength of mode E with increasing cylinder aspect ratio and incident angles were also mapped. A summary of the characteristics of the three-dimensional modes observed in this study is provided in table 1. The spanwise wavelengths of these modes increases with an increase in angle of incidence. In summary, a large region of the $\Gamma - Re - I$ parameter region was investigated for the flow past an elliptical cylinder, with several interesting flow features observed. The three-dimensional scenario for $I \leqslant 20^\circ$ is rich in fluid dynamics with several three-dimensional modes found to be unstable over a wide range of spanwise wavelengths.

Acknowledgements

The support from Australian Research Council (ARC) Discovery Grants DP130100822, DP150102879, DP150103177 and computing time from the National Computational Infrastructure (NCI), Victorian Life Sciences Computation Initiative (VLSCI) and Pawsey Supercomputing Centre are gratefully acknowledged. This research was also supported in part by the Monash e-Research Centre and eSolutions-Research Support Services through the use of the Monash Campus HPC Cluster and the Nectar Research Cloud. The authors would also like to acknowledge the storage space provided via VicNode/RDSI grant allocations 2014R8.2 and 2014R11.18.

Appendix A. Domain size study

Shown in table 2 is the domain size study at $\Gamma = 2, I = 0^\circ, Re = 440$. The values of the time-averaged drag coefficient ($\overline{C_d}$), root mean square of the lift coefficient ($C_{l,RMS}$) and Strouhal number (St) for the domain $60D \times 60D \times 100D$ (inlet $\times$ lateral $\times$ outlet) are within 1 % of the values for the $200D \times 200D \times 200D$ domain.

Inlet × Lateral × Outlet	$\overline{C_d}$	$C_{l,RMS}$	St
$60D \times 60D \times 100D$	0.806967	0.347251	0.214300
$100D \times 100D \times 100D$	0.805892	0.347854	0.214121
$200D \times 200D \times 200D$	0.804988	0.346622	0.214004

TABLE 2. Variation of time-averaged drag coefficient ($\overline{C_d}$), root mean square of the lift coefficient ($C_{l,RMS}$) and Strouhal number (St) with the specified domain sizes at $\Gamma = 2$, $I = 0°$, $Re = 440$.

N	$\overline{C_d}$	$C_{l,RMS}$	St
4	0.712217	0.291714	0.232481
5	0.710023	0.294918	0.231254
6	0.709486	0.293001	0.230951
7	0.709350	0.295065	0.230888
8	0.709194	0.292911	0.230847
9	0.709206	0.294625	0.230847
10	0.709173	0.294868	0.230809
11	0.709145	0.294655	0.230809

TABLE 3. Variation of time-averaged drag coefficient ($\overline{C_d}$), root mean square of the lift coefficient ($C_{l,RMS}$) and Strouhal number (St) with spatial resolution (N) at $\Gamma = 2.5$, $I = 0°$, $Re = 500$. A resolution of $N = 8$ was chosen for the computations and it is within 0.6 % of the maximum tested value at $N = 11$.

N	$\overline{C_d}$	$\overline{C_l}$	St
4	0.717410	0.745443	0.214365
5	0.717101	0.741692	0.214175
6	0.717220	0.740980	0.214114
7	0.717054	0.740122	0.214102
8	0.717125	0.740406	0.214134
9	0.717120	0.740516	0.214143
10	0.717096	0.740101	0.214134
11	0.717058	0.740159	0.214127

TABLE 4. Variation of time-averaged drag coefficient ($\overline{C_d}$), root mean square of the lift coefficient ($\overline{C_l}$) and Strouhal number (St) with spatial resolution (N) at $\Gamma = 2.5$, $I = 10°$, $Re = 500$. A resolution of $N = 8$ was chosen for the computations and it is within 0.5 % of the maximum tested value at $N = 11$.

Appendix B. Spatial resolution size study

Shown in tables 3–7 are the spatial resolution studies for the specified parametric values.

A convergence study was undertaken to ensure that the Floquet multipliers were accurate for the newly observed modes. Shown in table 6 are the Floquet multipliers for mode QPA at the specified parametric values. For each case, the domain sizes and time step used were fixed, and the number of internal node points (N) was varied.

A convergence study for the mode C instability was carried out at $\Gamma = 2$, $I = 20°$, $Re = 400$, $\lambda/D = 2.5$. Only the magnitude of the multiplier is shown in table 7.

N	$\overline{C_d}$	$\overline{C_l}$	St
4	0.795453	1.642686	0.187553
5	0.803145	1.642469	0.188037
6	0.803134	1.641160	0.188094
7	0.803370	1.641172	0.188138
8	0.797985	1.651956	0.188170
9	0.802877	1.639757	0.188183
10	0.799550	1.646020	0.188218
11	0.795732	1.661537	0.188195

TABLE 5. Variation of time-averaged drag coefficient ($\overline{C_d}$), root mean square of the lift coefficient ($\overline{C_l}$) and Strouhal number (St) with spatial resolution (N) at $\Gamma = 2.5$, $I = 20°$, $Re = 500$. A resolution of $N = 8$ was chosen for the computations and it is within 0.6 % of the maximum tested value at $N = 11$.

N	Re(μ)	Img(μ)	Magnitude (μ)
4	0.9733301103	0.2528498209	1.0056363834
5	0.9755267122	0.2463104741	1.0061417474
6	0.9753805470	0.2462380863	1.0059823093
7	0.9753642243	0.2460460034	1.0059194828
8	0.9752702964	0.2462427170	1.0058765464
9	0.9752566756	0.2462731594	1.0058707931
10	0.9752127922	0.2461762027	1.0058045102

TABLE 6. Variation of Real (Re(μ)) and imaginary components (Img(μ)) of the Floquet multiplier with spatial resolution (N) for mode QPA at $\Gamma = 2.5$, $I = 16°$, $Re = 260$, $\lambda/D = 3.9$. A resolution of $N = 8$ was chosen for the computations and it is within 0.007 % of the maximum tested value at $N = 10$.

N	Magnitude of the multiplier $\lvert\mu\rvert$
4	1.38205
5	1.48179
6	1.48877
7	1.48518
8	1.48492
9	1.48421
10	1.48193
11	1.48166

TABLE 7. Variation of magnitude of the Floquet multiplier with spatial resolution for mode C at $\Gamma = 2$, $I = 20°$, $Re = 400$, $\lambda/D = 2.5$. A resolution of $N = 8$ was chosen for the computations and it is within 0.22 % of the maximum tested value at $N = 11$.

REFERENCES

AKBAR, T., BOUCHET, G. & DUŠEK, J. 2011 Numerical investigation of the subcritical effects at the onset of three-dimensionality in the circular cylinder wake. *Phys. Fluids* **23** (9), 094103.

AKBAR, T., BOUCHET, G. & DUŠEK, J. 2014 Co-existence of A and B modes in the cylinder wake at $Re = 170$. *Eur. J. Mech. (B/Fluids)* **48**, 19–26.

BADR, H. M., DENNIS, S. C. R. & KOCABIYIK, S. 2001 Numerical simulation of the unsteady flow over an elliptic cylinder at different orientations. *Intl J. Numer. Meth. Fluids* **37** (8), 905–931.

BARKLEY, D. & HENDERSON, R. D. 1996 Three-dimensional Floquet stability analysis of the wake of a circular cylinder. *J. Fluid Mech.* **322**, 215–241.

BARKLEY, D., TUCKERMAN, L. S. & GOLUBITSKY, M. 2000 Bifurcation theory for three-dimensional flow in the wake of a circular cylinder. *Phys. Rev.* E **61**, 5247–5252.

BEHARA, S. & MITTAL, S. 2010 Flow past a circular cylinder at low Reynolds number: oblique vortex shedding. *Phys. Fluids* **22** (5), 054102.

BLACKBURN, H. M. & LOPEZ, J. M. 2003 On three-dimensional quasiperiodic Floquet instabilities of two-dimensional bluff body wakes. *Phys. Fluids* **15**, L57–L60.

BLACKBURN, H. M., MARQUES, F. & LOPEZ, J. M. 2005 Symmetry breaking of two-dimensional time-periodic wakes. *J. Fluid Mech.* **552**, 395–411.

BLACKBURN, H. M. & SHEARD, G. J. 2010 On quasiperiodic and subharmonic Floquet wake instabilities. *Phys. Fluids* **22** (3), 031701,1–4.

CANUTO, C., HUSSAINI, M. Y., QUARTERONI, A. & ZANG, T. A. 1988 *Spectral Methods in Fluid Dynamics*, 2nd edn. Springer.

CARMO, B. S., SHERWIN, S. J., BEARMAN, P. W. & WILLDEN, R. H. J. 2008 Wake transition in the flow around two circular cylinders in staggered arrangements. *J. Fluid Mech.* **597**, 1–29.

CHOI, C. B. & YANG, K. S. 2014 Three-dimensional instability in flow past a rectangular cylinder ranging from a normal flat plate to a square cylinder. *Phys. Fluids* **26** (6), 061702.

CHORIN, A. J. 1968 Numerical solution of the Navier–Stokes equations. *Maths Comput.* **22**, 745–762.

GRIFFITH, M. D., JACONO, D. L., SHERIDAN, J. & LEONTINI, J. S. 2016 Passive heaving of elliptical cylinders with active pitching – from cylinders towards flapping foils. *J. Fluids Struct.* **67**, 124–141.

GRIFFITH, M. D., THOMPSON, M. C., LEWEKE, T., HOURIGAN, K. & ANDERSON, W. P. 2007 Wake behaviour and instability of flow through a partially blocked channel. *J. Fluid Mech.* **582**, 319–340.

JACKSON, C. P. 1987 A finite-element study of the onset of vortex shedding in flow past variously shaped bodies. *J. Fluid Mech.* **182**, 23–45.

JIANG, H., CHENG, L., DRAPER, S. & AN, H. 2017 Two- and three-dimensional instabilities in the wake of a circular cylinder near a moving wall. *J. Fluid Mech.* **812**, 435–462.

JIANG, H., CHENG, L., DRAPER, S., AN, H. & TONG, F. 2016*a* Three-dimensional direct numerical simulation of wake transitions of a circular cylinder. *J. Fluid Mech.* **801**, 353–391.

JIANG, H., CHENG, L., TONG, F., DRAPER, S. & AN, H. 2016*b* Stable state of mode A for flow past a circular cylinder. *Phys. Fluids* **28** (10), 104103.

JOHNSON, S. A., THOMPSON, M. C. & HOURIGAN, K. 2004 Predicted low frequency structures in the wake of elliptical cylinders. *Eur. J. Mech. (B/Fluids)* **23** (1), 229–239.

JONES, M. C., HOURIGAN, K. & THOMPSON, M. C. 2015 A study of the geometry and parameter dependence of vortex breakdown. *Phys. Fluids* **27**, 044102.

JUNG, J. H. & YOON, H. S. 2014 Large eddy simulation of flow over a twisted cylinder at a subcritical Reynolds number. *J. Fluid Mech.* **759**, 579–611.

KARNIADAKIS, G. E., ISRAELI, M. & ORSZAG, S. A. 1991 High-order splitting methods for the incompressible Navier–Stokes equations. *J. Comput. Phys.* **97**, 414–443.

KARNIADAKIS, G. E. & SHERWIN, S. J. 2005 *Spectral/hp Methods for Computational Fluid Dynamics*. Oxford University Press.

KARNIADAKIS, G. E. & TRIANTAFYLLOU, G. S. 1992 Three-dimensional dynamics and transition to turbulence in the wake of bluff objects. *J. Fluid Mech.* **238**, 1–30.

KIM, M.-S. & PARK, Y.-B. 2006 Unsteady lift and drag forces acting on the elliptic cylinder. *J. Mech. Sci. Technol.* **20** (1), 167–175.

KIM, M.-S. & SENGUPTA, A. 2005 Unsteady viscous flow over elliptic cylinders at various thickness with different Reynolds numbers. *J. Mech. Sci. Technol.* **19** (3), 877–886.

KIM, W., LEE, J. & CHOI, H. 2016 Flow around a helically twisted elliptic cylinder. *Phys. Fluids* **28** (5), 053602.

LEONTINI, J. S., LO JACONO, D. & THOMPSON, M. C. 2015 Stability analysis of the elliptic cylinder wake. *J. Fluid Mech.* **763**, 302–321.

LEONTINI, J. S., THOMPSON, M. C. & HOURIGAN, K. 2007 Three-dimensional transition in the wake of a transversely oscillating cylinder. *J. Fluid Mech.* **577**, 79–104.

LINDSEY, W. F. 1937 Drag of cylinders of simple shapes. *Tech. Rep.* 619. National Advisory Committee for Aeronautics.

LING, G. C. & ZHAO, H. L. 2009 Vortex dislocations in wake-type flow induced by spanwise disturbances. *Phys. Fluids* **21** (7), 073604.

LUGT, H. J. & HAUSSLING, H. J. 1972 Laminar flows past elliptic cylinders at various angles of attack. *Tech. Rep.* 3748. Naval Ship Research And Development Center.

MAMUN, C. K. & TUCKERMAN, L. S. 1995 Asymmetry and Hopf-bifurcation in spherical Couette flow. *Phys. Fluids* **7** (1), 80–91.

MARQUES, F., LOPEZ, J. M. & BLACKBURN, H. M. 2004 Bifurcations in systems with Z_2 spatio-temporal and $O(2)$ spatial symmetry. *Physica D* **189**, 247–276.

MENEGHINI, J. R., CARMO, B. S., TSILOUFAS, S. P., GIORIA, R. S. & ARANHA, J. A. P. 2011 Wake instability issues: from circular cylinders to stalled airfoils. *J. Fluids Struct.* **27** (56), 694–701; IUTAM Symposium on Bluff Body Wakes and Vortex-Induced Vibrations (BBVIV-6).

MITTAL, R. & BALACHANDAR, S. 1996 Direct numerical simulation of flow past elliptic cylinders. *J. Comput. Phys.* **124** (2), 351–367.

MITTAL, S. & SIDHARTH, G. S. 2014 Steady forces on a cylinder with oblique vortex shedding. *J. Fluids Struct.* **44**, 310–315.

MORI, T., YOSHIKAWA, H. & OTA, T. 2003 Unsteady flow around an elliptic cylinder in the critical Reynolds number regime. In *Proceedings of the ASME Fluids Engineering Division Summer Meeting*, vol. 1, pp. 677–682.

NAIK, S. N., VENGADESAN, S. & PRAKASH, K. A. 2017 Numerical study of fluid flow past a rotating elliptic cylinder. *J. Fluids Struct.* **68**, 15–31.

NAIR, M. T. & SENGUPTA, T. K. 1997 Unsteady flow past elliptical cylinders. *J. Fluids Struct.* **11** (6), 555–595.

NAVROSE, M. J. & MITTAL, S. 2015 Three-dimensional flow past a rotating cylinder. *J. Fluid Mech.* **766**, 28–53.

NG, Z. Y., VO, T., HUSSAM, W. K. & SHEARD, G. J. 2016 Linear instabilities in the wakes of cylinders with triangular cross-sections. In *20th Australasian Fluid Mechanics Conference* (ed. N. Jones, G. Ivey, T. Zhou & S. Draper). Australasian Fluid Mechanics Society.

PAUL, I., PRAKASH, K. A. & VENGADESAN, S. 2014*a* Numerical analysis of laminar fluid flow characteristics past an elliptic cylinder: A parametric study. *Intl J. Numer. Meth. Heat Fluid Flow* **24** (7), 1570–1594.

PAUL, I., PRAKASH, K. A. & VENGADESAN, S. 2014*b* Onset of laminar separation and vortex shedding in flow past unconfined elliptic cylinders. *Phys. Fluids* **26** (2), 023601,1–15.

RADI, A., THOMPSON, M. C., RAO, A., HOURIGAN, K. & SHERIDAN, J. 2013 Experimental evidence of new three-dimensional modes in the wake of a rotating cylinder. *J. Fluid Mech.* **734**, 567–594.

RAO, A., LEONTINI, J. S., THOMPSON, M. C. & HOURIGAN, K. 2013*a* Three-dimensionality in the wake of a rotating cylinder in a uniform flow. *J. Fluid Mech.* **717**, 1–29.

RAO, A., LEONTINI, J. S., THOMPSON, M. C. & HOURIGAN, K. 2013*b* Three-dimensionality in the wake of a rapidly rotating cylinder in uniform flow. *J. Fluid Mech.* **730**, 379–391.

RAO, A., PASSAGGIA, P.-Y., BOLNOT, H., THOMPSON, M. C., LEWEKE, T. & HOURIGAN, K. 2012 Transition to chaos in the wake of a rolling sphere. *J. Fluid Mech.* **695**, 135–148.

RAO, A., RADI, A., LEONTINI, J. S., THOMPSON, M. C., SHERIDAN, J. & HOURIGAN, K. 2015*a* A review of rotating cylinder wake transitions. *J. Fluids Struct.* **53**, 2–14; special issue on unsteady separation in fluid-structure interaction – II.

RAO, A., RADI, A., LEONTINI, J. S., THOMPSON, M. C., SHERIDAN, J. & HOURIGAN, K. 2015*b* The influence of a small upstream wire on transition in a rotating cylinder wake. *J. Fluid Mech.* **769**, R2-1–R2-12.

RAO, A., STEWART, B. E., THOMPSON, M. C., LEWEKE, T. & HOURIGAN, K. 2011 Flows past rotating cylinders next to a wall. *J. Fluids Struct.* **27** (5–6), 668–679.

RAO, A., THOMPSON, M. C., LEWEKE, T. & HOURIGAN, K. 2013*c* The flow past a circular cylinder translating at different heights above a wall. *J. Fluids Struct.* **41** (0), 9–21.

RAO, A., THOMPSON, M. C. & HOURIGAN, K. 2016 A universal three-dimensional instability of the wakes of two-dimensional bluff bodies. *J. Fluid Mech.* **792**, 50–66.

RAO, A., THOMPSON, M. C., LEWEKE, T. & HOURIGAN, K. 2015*c* Flow past a rotating cylinder translating at different gap heights along a wall. *J. Fluids Struct.* **57**, 314–330.

ROBICHAUX, J., BALACHANDAR, S. & VANKA, S. P. 1999 Three-dimensional Floquet instability of the wake of a square cylinder. *Phys. Fluids* **11** (3), 560–578.

RYAN, K., THOMPSON, M. C. & HOURIGAN, K. 2005 Three-dimensional transition in the wake of bluff elongated cylinders. *J. Fluid Mech.* **538**, 1–29.

SHEARD, G. J. 2007 Cylinders with elliptical cross-section: wake stability with incidence angle variation. In *Proceedings of the IUTAM Symposium on Unsteady Separated Flows and Their Control*, pp. 5–18. Institut de Mécanique des Fluides de Toulouse.

SHEARD, G. J. 2011 Wake stability features behind a square cylinder: focus on small incidence angles. *J. Fluids Struct.* **27** (5–6), 734–742.

SHEARD, G. J., FITZGERALD, M. J. & RYAN, K. 2009 Cylinders with square cross-section: wake instabilities with incidence angle variation. *J. Fluid Mech.* **630**, 43–69.

SHEARD, G. J., THOMPSON, M. C. & HOURIGAN, K. 2004*a* Asymmetric structure and non-linear transition behaviour of the wakes of toroidal bodies. *Eur. J. Mech. (*B*/Fluids)* **23** (1), 167–179.

SHEARD, G. J., THOMPSON, M. C. & HOURIGAN, K. 2004*b* From spheres to circular cylinders: non-axisymmetric transitions in the flow past rings. *J. Fluid Mech.* **506**, 45–78.

SHEARD, G. J., THOMPSON, M. C. & HOURIGAN, K. 2005*a* Subharmonic mechanism of the mode C instability. *Phys. Fluids* **17** (11), 1–4.

SHEARD, G. J., THOMPSON, M. C., HOURIGAN, K. & LEWEKE, T. 2005*b* The evolution of a subharmonic mode in a vortex street. *J. Fluid Mech.* **534**, 23–38.

STEWART, B. E., HOURIGAN, K., THOMPSON, M. C. & LEWEKE, T. 2006 Flow dynamics and forces associated with a cylinder rolling along a wall. *Phys. Fluids* **18** (11), 111701,1–4.

STEWART, B. E., THOMPSON, M. C., LEWEKE, T. & HOURIGAN, K. 2010 The wake behind a cylinder rolling on a wall at varying rotation rates. *J. Fluid Mech.* **648**, 225–256.

STROUHAL, V. 1878 Ueber eine besondere art der tonerregung. *Annalen der Physik* **241** (10), 216–251.

THOMPSON, M. C. & HOURIGAN, K. 2003 The sensitivity of steady vortex breakdown bubbles in confined cylinder flows to rotating lid misalignment. *J. Fluid Mech.* **496**, 129–138.

THOMPSON, M. C., HOURIGAN, K., CHEUNG, A. & LEWEKE, T. 2006*a* Hydrodynamics of a particle impact on a wall. *Appl. Math. Model.* **30**, 1356–1369.

THOMPSON, M. C., HOURIGAN, K., RYAN, K. & SHEARD, G. J. 2006*b* Wake transition of two-dimensional cylinders and axisymmetric bluff bodies. *J. Fluids Struct.* **22**, 793–806.

THOMPSON, M. C., HOURIGAN, K. & SHERIDAN, J. 1996 Three-dimensional instabilities in the wake of a circular cylinder. *Exp. Therm. Fluid Sci.* **12**, 190–196.

THOMPSON, M. C., RADI, A., RAO, A., SHERIDAN, J. & HOURIGAN, K. 2014 Low-Reynolds-number wakes of elliptical cylinders: from the circular cylinder to the normal flat plate. *J. Fluid Mech.* **751**, 570–600.

WEI, D. J., YOON, H. S. & JUNG, J. H. 2016 Characteristics of aerodynamic forces exerted on a twisted cylinder at a low Reynolds number of 100. *Comput. Fluids* **136**, 456–466.

WILLIAMSON, C. H. K. 1988 The existence of two stages in the transition to three-dimensionality of a cylinder wake. *Phys. Fluids* **31**, 3165–3168.

WILLIAMSON, C. H. K. 1989 Oblique and parallel modes of vortex shedding in the wake of a circular cylinder at low Reynolds numbers. *J. Fluid Mech.* **206**, 579–627.

WILLIAMSON, C. H. K. 1992 The natural and forced formation of spot-like in the transition of a wake. *J. Fluid Mech.* **243**, 393–441.

WILLIAMSON, C. H. K. 1996*a* Three-dimensional wake transition. *J. Fluid Mech.* **328**, 345–407.

WILLIAMSON, C. H. K. 1996*b* Vortex dynamics in the cylinder wake. *Annu. Rev. Fluid Mech.* **28**, 477–539.

YANG, D., PETTERSEN, B., ANDERSSON, H. I. & NARASIMHAMURTHY, V. D. 2012 Vortex shedding in flow past an inclined flat plate at high incidence. *Phys. Fluids* **24** (8), 084103.

YANG, D., PETTERSEN, B., ANDERSSON, H. I. & NARASIMHAMURTHY, V. D. 2013 Floquet stability analysis of the wake of an inclined flat plate. *Phys. Fluids* **25** (9), 094103.

YILDIRIM, I., RINDT, C. C. M. & VAN STEENHOVEN, A. A. 2013*a* Energy contents and vortex dynamics in Mode-C transition of wired-cylinder wake. *Phys. Fluids* **25** (5), 054103.

YILDIRIM, I., RINDT, C. C. M. & VAN STEENHOVEN, A. A. 2013*b* Mode C flow transition behind a circular cylinder with a near-wake wire disturbance. *J. Fluid Mech.* **727**, 30–55.

YOON, H. S., YIN, J., CHOI, C., BALACHANDAR, S. & HA, M. Y. 2016 Bifurcation of laminar flow around an elliptic cylinder at incidence for low Reynolds numbers. *Prog. Comput. Fluid Dyn.* **16** (3), 163–178.

ZHANG, H.-Q., FEY, U., NOACK, B. R., KONIG, M. & ECKELEMANN, H. 1995 On the transition of the cylinder wake. *Phys. Fluids* **7** (4), 779–794.

ZIENKIEWICZ, O. C. 1977 *The Finite Element Method*, 3rd edn. McGraw-Hill.